

# Universal resource-efficient topological measurement-based quantum computation via color-code-based cluster states

Seok-Hyung Lee and Hyunseok Jeong

*Department of Physics and Astronomy, Seoul National University, Seoul 08826, Republic of Korea*

Topological measurement-based quantum computation (MBQC) enables one to carry out universal fault-tolerant quantum computation via single-qubit Pauli measurements with a family of large entangled states called cluster states as resources. Raussendorf's three-dimensional cluster states (RTCSs) based on the surface codes are mainly concerned for topological MBQC, but costly state distillation is required to fault-tolerantly implement the logical Hadamard, phase, and  $\pi/8$  ( $T$ ) gates which are essential for building up arbitrary logical gates. We suggest a family of cluster states called color-code-based cluster states (CCCSs) based on the two-dimensional color codes instead of the surface codes. We describe the fault-tolerant MBQC scheme via CCCSs by defining logical qubits, constructing elementary logical gates, and suggesting error correction schemes. We show that not only the logical controlled-not gate but also the logical Hadamard and phase gates can be implemented fault-tolerantly without state distillation, although the fault-tolerant logical  $T$  gate still requires it. We further prove that the minimal number of physical qubits per logical qubit in a CCCS is at most approximately 1.8 times smaller than the case of a RTCS. We lastly show that the error threshold of MBQC via CCCSs for logical-Z errors is approximately 3.0%, which is comparable to the value for RTCSs, assuming a simple error model where physical qubits have  $Z$  or  $X$ -measurement errors independently with the same probability.

## I. INTRODUCTION

Three major theoretical challenges for quantum computation (QC) are *universality*, *fault-tolerance*, and *resource-efficiency*. Universality indicates the ability of a quantum computer to initialize logical qubits to the computational basis and perform any unitary gate on them. It is known that the controlled-not (CNOT), Hadamard, and phase gates completely generate the Clifford group, and together with the  $\pi/8$  ( $T$ ) gate, any unitary operation may be approximated to an arbitrary accuracy [1, 2].

To achieve fault-tolerance, various quantum error-correcting (QEC) codes have been proposed from simple codes with few physical qubits [3–7] to topological stabilizer codes defined on lattice structures of qubits allowing only local interactions which are easily scalable [8], and demonstrated experimentally in assorted systems for small code distances [9–17]. Particularly, the *surface codes* [18–25], a family of topological codes defined on two-dimensional (2D) lattices, have high error thresholds up to about 12% [24], thus they are one of the most promising candidates for fault-tolerant QC. The *2D color codes* is another family of topological codes [8, 26, 27] which enable transversal<sup>1</sup> implementation of the logical CNOT, Hadamard, and phase gates thanks to their self-duality. Moreover, three-dimensional (3D) gauge color

codes even allow transversal implementation of the logical  $T$  gate as well as the Clifford gates, thus have been getting much attention recently [28–35].

Lastly, fault-tolerant QC typically requires enormous resource overhead, which makes it tough to realize it. It is not only because a single logical qubit is composed of multiple physical qubits, but also because state distillation for non-Clifford gates and sometimes for several Clifford gates demand many ancillary logical qubits [22, 24, 36, 37], e.g., one round of a typical protocol to distill an  $|A_L\rangle := \frac{1}{\sqrt{2}}(|0_L\rangle + e^{i\pi/4}|1_L\rangle)$  state for the logical  $T$  gate requires 15 ancillary logical qubits [24, 36, 38].

*Measurement-based QC* (MBQC) is an alternative of conventional circuit-based QC (CBQC), processed only by single-qubit Pauli measurements with a family of large entangled states called *cluster states* as resources [38–43]. The ingredients for generating Cluster states are physical qubits initialized to the  $X$  basis and controlled- $Z$  (CZ) gates on them, thus MBQC requires much fewer types of physical-level operations than typical CBQC. The initial MBQC schemes via cluster states on 2D planes [39, 40] were universal but not fault-tolerant. To achieve fault-tolerance, the space should be 3D; *Raussendorf's 3D cluster states* (RTCSs) allow universal and fault-tolerant MBQC with topologically-encoded logical qubits [38, 41–43]. Additionally, it was shown that it can tolerate imperfect preparation of cluster states such as qubits losses or failed CZ gates [44–46]. MBQC via cluster states is regarded as one of the suitable candidates for practical fault-tolerant QC, especially in optical systems [46–57].

MBQC via RTCSs is powerful from the point of view of universality and fault-tolerance, but has a significant drawback: there are no direct ways to fault-tolerantly implement the logical Hadamard, phase, and  $T$  gates without costly state distillation, unlike the logical CNOT gate [38, 41–43]. To solve this problem, we consider re-

<sup>1</sup> That a logical gate  $U$  is transversal means that  $U$  can be expressed as  $U = U_1 U_2 \dots$  such that a unitary operator  $U_i$  acts only on the  $i$ th physical qubit for each logical qubit for all  $i$ 's. For example, if  $X_L := X_1 \dots X_n$  for  $[[n, 1, d]]$  code where  $X_i$  is the  $X$  operator on the  $i$ th physical qubit,  $X_L$  is transversal. Specific 2D color codes implement the logical Hadamard gate by the combination of the Hadamard gate on every physical qubit, and similarly for the logical phase gate [26, 27].

cent studies on generalizing the relation between RTCSs and surface codes to any Calderbank-Steane-Shor (CSS) codes [58, 59] and later to any stabilizer codes [60]. We also consider Ref. [27] on 2D color code computation introducing “defects” for logical operations, since a similar approach on the surface codes leads to the protocol for MBQC via RTCSs. Motivated by these works, we propose a new MBQC scheme via a family of cluster states based on the 2D color codes instead of the surface codes, called *color-code-based cluster states* (CCCSs).

Throughout this paper, we show that MBQC via CCCSs is a competitive candidate on realistic QC, regarding the three challenges mentioned at the very first. We describe the fault-tolerant implementation of the logical CNOT, Hadamard, and phase gates without state distillation, unlike MBQC via RTCSs, although the logical  $T$  gate still requires it. We then prove that it requires a smaller amount of physical qubits per logical qubits than the case of RTCSs, which makes it resource-efficient even more. Finally, we show that they have a similar level of fault-tolerance by comparing their error thresholds.

This paper is structured as follows. In Sec. II, we review the concept of cluster states and the general process of MBQC. In Sec. III, we construct CCCSs and describe their properties, especially about their stabilizers called *correlation surfaces*. In Sec. IV, we define logical qubits and suggest the schemes for their initialization and measurements, elementary logical gates, and state injection for state distillation. In Sec. V, we present the methods for error correction. In Sec. VI, we calculate resource overhead and error thresholds of MBQC via CCCSs and compare them with the results for RTCSs. We conclude with final remarks in Sec. VII.

## II. CLUSTER STATES AND MEASUREMENT-BASED QUANTUM COMPUTATION

For defining a *cluster state*, we consider a graph  $G = (V, E)$ , where  $V$  and  $E$  are the sets of vertices and edges, respectively. A cluster state is constructed by attaching a qubit to every vertex in  $V$ , initializing them to the  $|+\rangle$  states where  $|\pm\rangle := (|0\rangle \pm |1\rangle)/\sqrt{2}$ , then applying a controlled- $Z$  (CZ) gate on every pair of qubits connecting by an edge in  $E$ . The constructed cluster state has a stabilizer generator (SG)  $S(v)$  for each vertex  $v \in V$  defined as

$$S(v) := X(v) \prod_{v' \in V: (v, v') \in E} Z(v'), \quad (1)$$

where  $X(v)$  and  $Z(v)$  are the  $X$  and  $Z$  operators, respectively, on the qubit at the vertex  $v$  denoted by  $Q(v)$ . We say that  $S(v)$  is *around*  $v$  or  $Q(v)$ , called its *center vertex* or *qubit*, respectively. Examples of cluster states are presented in Fig. 1.

For MBQC, modified versions of cluster states are used, where some qubits do not need to be initialized

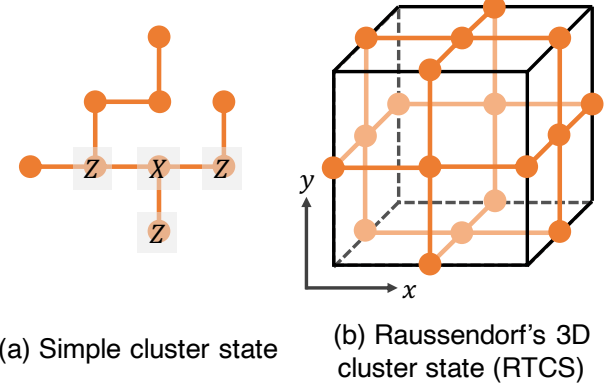


FIG. 1. Examples of cluster states. Orange dots and lines indicate vertices and edges of the graphs, respectively. To construct a cluster state, qubits initialized to the  $|+\rangle = \frac{1}{\sqrt{2}}(|0\rangle + |1\rangle)$  states are placed on the vertices, then a CZ gate is applied on the qubits connected by each edge. (a) A cluster state on a simple graph. The presented “XZZZ” operator indicates an example of a stabilizer generator given in Eq. (1). (b) A unit cell of a Raussendorf’s 3D cluster state (RTCS). A vertex is located on each edge and face of the cell.

to the  $|+\rangle$  states.  $S(v)$  where  $Q(v)$  is each of such qubits is then no longer a stabilizer, but others still remain as SGs.

General MBQC via a cluster state to implement a quantum circuit is processed through the following three steps [38–40, 42, 43]:

1. *Preparation.* For a given graph  $G(V, E)$ , a qubit is attached to each vertex.  $Q(V)$  is divided into three subsets: the input qubits  $Q_{\text{IN}}$ , the output qubits  $Q_{\text{OUT}}$ , and the others.  $Q_{\text{OUT}} = \emptyset$  if the desired circuit does not produce any output state or ends with measurements. The input logical states are prepared in  $Q_{\text{IN}}$ . All qubits except those in  $Q_{\text{IN}}$  are initialized to the  $|+\rangle$  states. A CZ gate is then applied on every pair of qubits connected by an edge.
2. *Measurement.* For each physical qubit except those in  $Q_{\text{OUT}}$ , a single-qubit Pauli measurement, selected by a *measurement pattern* with a classical computer, is performed. The measurement pattern is determined by the desired circuit. Let the measurement results be  $M$ . If possible, errors in  $M$  are corrected by decoding the *parity-check* outcomes.
3. *Obtaining the results.* The output logical state is obtained from  $Q_{\text{OUT}}$  up to logical Pauli operators called *byproduct operators* determined by  $M$ . If  $Q_{\text{OUT}} = \emptyset$ , the results of the final logical measurements are determined by  $M$ .

Note that the preparation and measurement steps may be performed simultaneously; after a qubit  $q$  and its neighbors are prepared and CZ gates are applied on them,

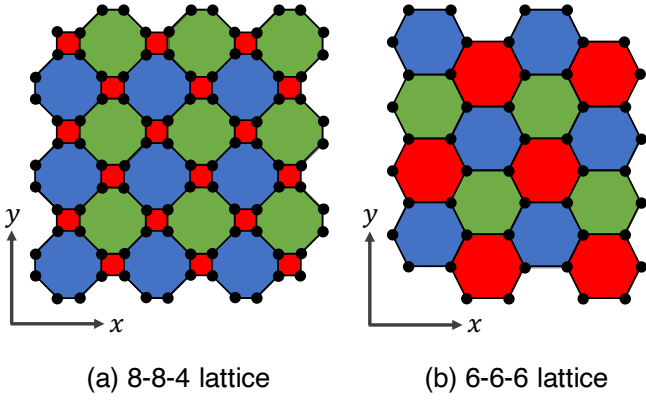


FIG. 2. Two typical examples of color-code lattices: the (a) 8-8-4 and (b) 6-6-6 lattices. The lattices are 3-valent and have 3-colorable faces.

it is allowed that  $q$  is measured before the other qubits are prepared. One of the spatial axes may be regarded as the *simulating time axis*, or simply the *time axis*, along which qubits are prepared and then measured in order. It is thus possible to minimize the number of unmeasured physical qubits in a moment by measuring each qubit as soon as possible after preparing it.

The cores of MBQC are the structure of the cluster state and the measurement pattern. We illustrate them one by one over the next two sections.

### III. COLOR-CODE-BASED CLUSTER STATES

In this section, we define color-code-based cluster states and describe their properties. Based on the work on the foliation of CSS codes [58], we consider a particular family of cluster states derived from a 2D color-code lattice, called *color-code-based cluster states* (CCCSs).

#### A. Two-dimensional color-code lattices

We first present 2D color-code lattices on which CCCSs are based. We consider a lattice  $\mathcal{L}_{2D}$  on a 2D plane which is 3-valent and has 3-colorable faces; namely, three edges meet at each vertex and one of the three colors (red, green, or blue) is assigned to each face in such a way that neighboring faces have different colors. Note that each edge, called *link*, is also colorable with the color of the faces it connects. Two typical examples (8-8-4 and 6-6-6) of such lattices are shown in Fig. 2. In the original 2D color codes, a qubit is attached to each vertex and two SGs ( $X$ - and  $Z$ -type) correspond to each face. Details on the codes are described in Ref. [8, 26].

Regarding a color-code lattice  $\mathcal{L}_{2D}$ , three *shrunk lattices* are defined, one for each color by shrinking all the faces of that color, as shown in Fig. 3. For example, in the red shrunk lattice, each vertex corresponds to a red

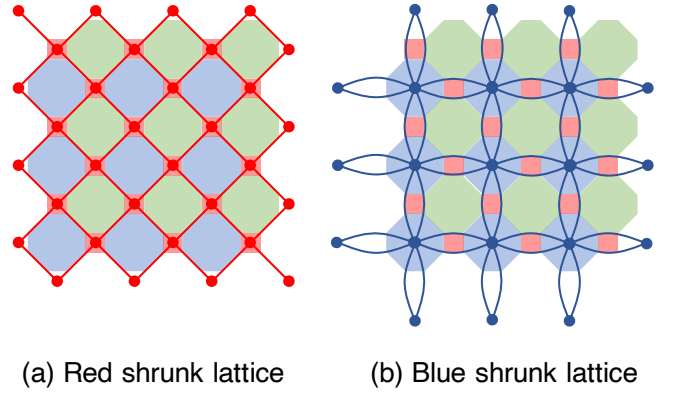


FIG. 3. (a) Red and (b) blue shrunk lattices of the 8-8-4 color-code lattice. Red or blue dots (lines) indicate their vertices (edges), which corresponds to red or blue faces (links) of the original lattices.

face in  $\mathcal{L}_{2D}$  and each face corresponds to a blue or green face in  $\mathcal{L}_{2D}$ . Edges of the red shrunk lattice then correspond to red links in  $\mathcal{L}_{2D}$ . The blue and green shrunk lattices are also defined analogously.

#### B. Construction of color-code-based cluster states

The graph  $G$  for a CCCS based on a color-code lattice  $\mathcal{L}_{2D}$  has a 3D structure composed of multiple identical 2D layers stacked along the simulating time axis.

The structure of each layer is originated from  $\mathcal{L}_{2D}$ , as illustrated in Fig. 4(a) for the case of the 8-8-4 lattice. Each vertex in the layer is located at either a vertex of  $\mathcal{L}_{2D}$  or the center of a face of  $\mathcal{L}_{2D}$ ; the corresponding qubit is called a *code qubit* (CQ) or an *ancilla qubit* (AQ), respectively. Each AQ is colorable with the color of the corresponding face in  $\mathcal{L}_{2D}$ . For each face in  $\mathcal{L}_{2D}$ , the layer has an edge connecting the corresponding AQ and each surrounding CQ, on which a CZ gate is applied. Each pair of CQs connected by a link in  $\mathcal{L}_{2D}$  is called *link* here as well. Note that links are not edges of  $G$ .

Next, we stack multiple identical layers along the time axis as shown in Fig. 4(b). Every pair of CQs adjacent along the time axis is connected by an edge in  $G$ . The vertices (CQs and AQs) and edges (between CQs and AQs in the same layer and between CQs in the adjacent layers) constructed above finally complete the graph  $G$  of the cluster state.

We assign each layer, qubit or link a “primality”: either *primal* or *dual*. Each layer is primal (dual) if it has an even (odd) time. An AQ is primal (dual) if it is in a primal (dual) layer, while a CQ or link is primal (dual) if it is in a dual (primal) layer. We label each qubit or link in an abbreviated form with its primality (“p” for primal and “d” for dual), color (“r” for red, “g” for green, and “b” for blue; omitted for CQs), and type (“AQ,” “CQ,” and “L” for a link). For example, a pgAQ means a primal

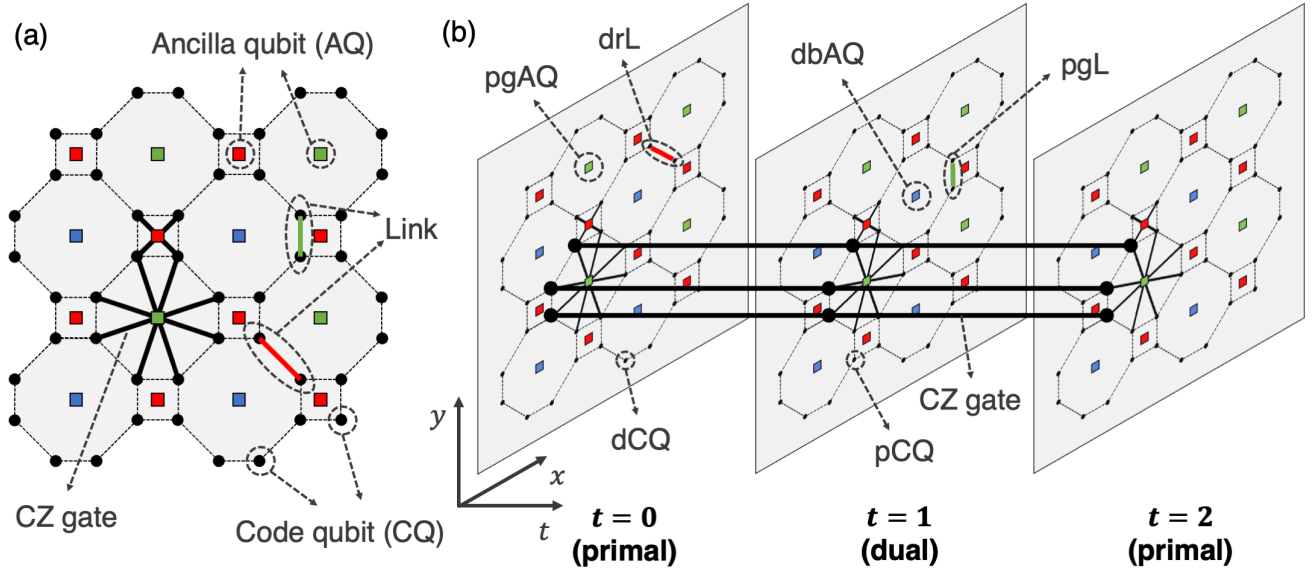


FIG. 4. Structure of a color-code-based cluster state (CCCS) based on the 8-8-4 color-code lattice  $\mathcal{L}_{2D}$ . (a) Structure of a single layer. Each black circle is a code qubit (CQ) located at a vertex of  $\mathcal{L}_{2D}$ . Each colored square is an ancilla qubit (AQ) with that color, located at the center of a face of  $\mathcal{L}_{2D}$  with that color. Each AQ is connected with surrounding CQs by edges (CZ gates), some of which are drawn as black solid lines. Two adjacent CQs are connected by a link, some of which are drawn as colored lines. (b) Stack of multiple identical layers along the simulating time axis. Each pair of two CQs adjacent along the time axis is connected by an edge, some of which are presented as black solid lines. One of the primalities (“primal” and “dual”) is alternatively assigned to each layer. An AQ (a CQ or link) is primal (dual) if it is in a primal layer, and vice versa for a dual layer. Labels of some elements defined in Sec. III B are shown.

green ancilla qubit. We also frequently use “c” instead of a specific color (r, g, or b) for a variable on colors.

### C. Stabilizer generators

We now present stabilizer generators (SGs) of a CCCS. Remark that, for each vertex  $v$  in  $G$ ,  $S(v)$  given in Eq. (1) is a SG if  $Q(v)$  is initialized to  $|+\rangle$ . We define *A*- and *C*-type SGs shown in Fig. 5(a) and (b) as follows.

**Definition 1 (A- and C-type SGs).** *An A- or C-type SG is the SG given in Eq. (1) around an AQ or a CQ, respectively.*

The support<sup>2</sup> of a C-type SG is distributed in three adjacent layers, while that of an A-type SG is contained in a layer.

Although these two types of SGs completely generate the stabilizer group, we need another two types of SGs: *L*- and *J*-type SGs in Fig. 5(c) and (d).

**Definition 2 (L-type SG).** *The L-type SG around a link  $l$  is the product of two C-type SGs whose center qubits constitute  $l$ .*

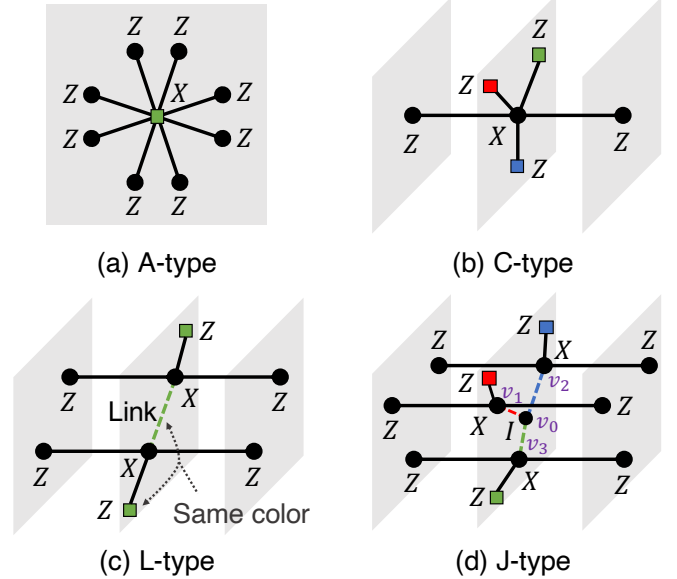


FIG. 5. Four types of stabilizer generators (SGs) in a CCCS defined in Definition 1–3: (a) A-, (b) C-, (c) L-, and (d) J-type. Each grey square indicates a layer. A SG of each type is the tensor product of the marked X or Z operators on the qubits.

<sup>2</sup> The support of an operator  $O$ , written as  $\text{supp}(O)$ , is the set of qubits on which  $O$  applies non-trivially.

**Definition 3 (J-type SG).** *Let  $S_i := S(v_i)$  for each  $i \in \{0, 1, 2, 3\}$  be a C-type SG such that  $(v_0, v_1), (v_0, v_2),$*

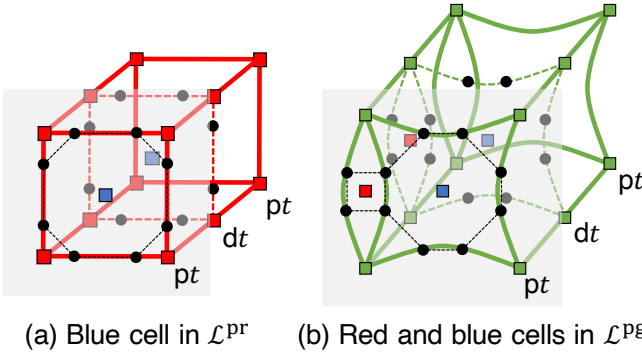


FIG. 6. Unit cells of the primal shrunk lattices of an 8-8-4 CCCS: (a) a blue cell in the primal red shrunk lattice  $\mathcal{L}^{\text{pr}}$  (a green cell is identical except the colors of AQs) and (b) red and blue cells in the primal green shrunk lattice  $\mathcal{L}^{\text{pg}}$ .  $\text{pts}$  and  $\text{dts}$  indicate primal and dual layers, respectively. Some qubits on the last layer are not displayed. All the pcAQs are vertices of  $\mathcal{L}^{\text{pc}}$ . Each spacelike (or timelike) edge, visualized as red or green solid lines, connects two adjacent vertices in a layer (or different layers) and corresponds to a pcL (or dcAQ). Faces and cells are defined naturally with the edges.

and  $(v_0, v_3)$  are links with different colors.  $S_I := S_1 S_2 S_3$  is then the J-type SG around the CQ  $Q(v_0)$ .

A-, L-, and J-type SGs together generate the stabilizer group overcompletely. To see this, regarding a J-type SG  $S_I$ , we consider an L-type SG  $S_{L_i} := S_0 S_i$  for each  $i \in \{0, 1, 2, 3\}$ , where  $S_i$ 's are defined in Definition 3. Then  $S_0 = S_{L_1} S_{L_2} S_{L_3} S_I$  holds, thus any C-type SG can be written as the product of L- and J-type SGs.

Let the  $P$ -support  $\text{supp}_P(O)$  of a multi-qubit Pauli operator  $O$  for  $P \in \{X, Y, Z\}$  be the subset of  $\text{supp}(O)$  corresponding to the  $P$  operator. Note that, for every SG regardless of its type, qubits in its  $X$ - and  $Z$ -support always have different primalities.

#### D. Shrunk lattices and correlation surfaces

Almost every discussion from now on is symmetric between the two primalities. Thus, throughout the rest of this paper, we frequently discuss only one of them, which implies that the other side can be treated similarly.

We now construct the shrunk lattices of a CCCS, which are analogous to those of the 2D color codes in Fig. 3. We then define correlation surfaces [38, 41, 42] within each shrunk lattice, through which logical gates are built for MBQC.

The primal c-colored shrunk lattice  $\mathcal{L}^{\text{pc}}$  is a 3D lattice containing every pcAQ as a vertex. Note that the vertices are only in primal layers. There are two types of edges connecting them: “spacelike” and “timelike” edges. Each spacelike edge corresponds to a pcL and connects two vertices in a layer. Each timelike edge connects two vertices adjacent along the time axis and contains a dcAQ

between them. Faces and cells are then naturally defined by the vertices and edges. Cells in each primal shrunk lattice are visualized in Fig. 6 for 8-8-4 CCCSs. Note that each primal layer in  $\mathcal{L}^{\text{pc}}$  is identical with the c-colored shrunk lattice of the 2D color code on which the CCCS is based.

Each element (vertex, edge, face, or cell) in a shrunk lattice corresponds to an AQ or a link, as presented in Table I. Here  $Q(b)$  for an element  $b$  denotes the set of qubits corresponding to  $b$ . Note that an element  $b$  is colorable with the color of the qubits in  $Q(b)$ . In particular, cells and spacelike faces have colors different from the color of the shrunk lattice, e.g.,  $\mathcal{L}^{\text{pr}}$  is composed of green and blue cells.

We now regard the shrunk lattices as chain complexes [38, 41, 42]. Let  $\mathcal{B}_i^{\text{pc}}$  for  $i = 0, 1, 2$ , or 3 be a set of vertices, edges, faces, or cells in  $\mathcal{L}^{\text{pc}}$ , respectively. We then consider a vector space  $H_i^{\text{pc}}$  generated by  $\mathcal{B}_i^{\text{pc}}$  over  $\mathbb{Z}_2$ . Each primal shrunk lattice may be regarded as a chain complex:  $\mathcal{L}^{\text{pc}} = \{H_3^{\text{pc}}, H_2^{\text{pc}}, H_1^{\text{pc}}, H_0^{\text{pc}}\}$ . Each element  $h_i \in H_i^{\text{pc}}$  is called an  $i$ -chain and corresponds to a set  $B(h_i) \subseteq \mathcal{B}_i^{\text{pc}}$  where each  $b \in B(h_i)$  has nonzero contribution in  $h_i$ . For example, if  $f_1$ ,  $f_2$ , and  $f_3$  are faces in  $\mathcal{L}_2^{\text{pc}}$ ,  $h_2 := f_1 + f_2 + f_3$  is a 2-chain in  $H_2^{\text{pc}}$  and  $B(h_2) = \{f_1, f_2, f_3\}$  holds. The correspondence is one-to-one, thus we do not distinguish  $h_i$  and  $B(h_i)$  from now on if it is not confusing. The chain complex  $\mathcal{L}^{\text{pc}}$  has a boundary map  $\partial$  which maps  $h_i \in H_i^{\text{pc}}$  to  $\partial h_i \in H_{i-1}^{\text{pc}}$  corresponding to the geometrical boundary of  $h_i$ . Note that  $\partial$  is a linear map and satisfies  $\partial \circ \partial = 0$ .

For an  $i$ -chain  $h_i$  and  $P \in \{X, Y, Z\}$ , we define a multi-qubit Pauli operator  $P(h_i)$  by

$$P(h_i) := \bigotimes_{q \in Q(h_i)} P(q),$$

where  $Q(h_i) := \bigcup_{b_i \in h_i} Q(b_i)$  and  $P(q)$  is the  $P$  operator on the qubit  $q$ . We now define correlation surfaces (CSs), essential elements for constructing logical operations through MBQC.

**Definition 4 (Correlation surface).** For each 2-chain  $h_2 \in H_2^{\text{p(d)c}}$ , the operator

$$S_{\text{CS}}(h_2) := X(h_2)Z(\partial h_2). \quad (2)$$

TABLE I. Qubits corresponding to each element (vertex, edge, face, or cell) in  $\mathcal{L}^{\text{pc}}$ . The results for  $\mathcal{L}^{\text{dc}}$  can be obtained by changing each p or d.

Element $b$ in $\mathcal{L}^{\text{pc}}$	Qubits $Q(b)$	
Vertex ( $\in \mathcal{B}_0^{\text{c}}$ )	pcAQ	dcAQ
Edge ( $\in \mathcal{B}_1^{\text{c}}$ )	Timelike	dcl (two dcQs)
Face ( $\in \mathcal{B}_2^{\text{c}}$ )	Spacelike	pcl (two pcQs)
Cell ( $\in \mathcal{B}_3^{\text{c}}$ )	Timelike	pc'AQ ( $c' \neq c$ )
	Spacelike	dc'AQ ( $c' \neq c$ )

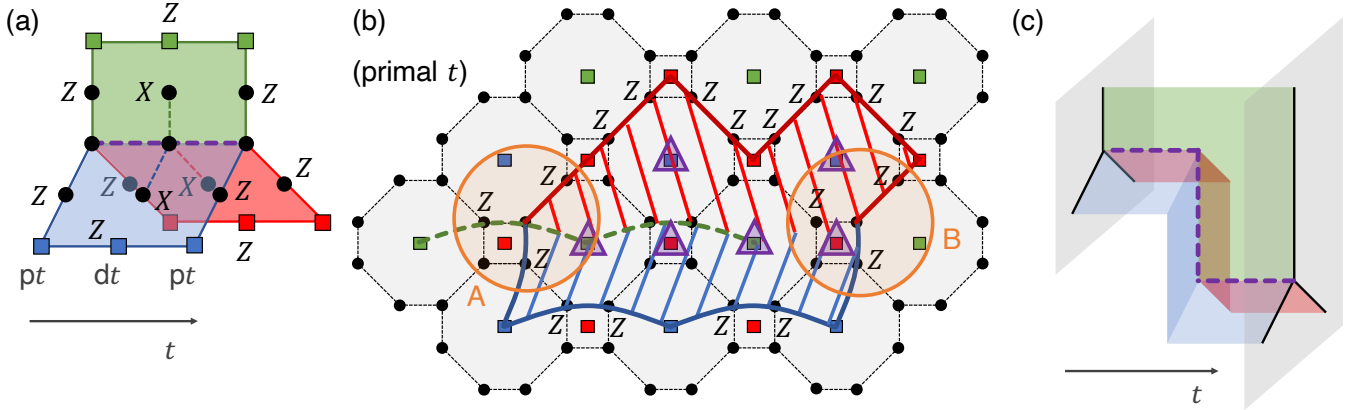


FIG. 7. (a) Timelike joint of primal correlation surfaces (CSs) originated from a J-type SG. The  $X$  or  $Z$  operators on the qubits indicate the support of the resulting CS. A series of CQs along which the three faces meet is marked as a purple dashed line. (b) Example of the construction of a spacelike joint of three primal CSs. A primal layer of an 8-8-4 CCCS is presented. We first assume a timelike pg-CS  $S$  ending at the green dashed line. We then expand  $S$  by multiplying the A-type SGs around the pAQs marked with purple triangles. After the expansion,  $\text{supp}_X(S)$  contains the marked pAQs, and  $\text{supp}_Z(S)$  contains the CQs along the red and blue solid lines. The area above (below) the green line can be regarded as a pr(b)-CS, in the sense that it may be expanded by multiplying ordinary pr(b)-CSs. A joint of the three CSs is thus constructed, and  $S$  is the corresponding joined CS. The qubits in  $\text{supp}_Z(S)$  inside the area A or B exactly match with the final layer of a timelike joint, thus spacelike and timelike joints may be connected. (c) Example of a general joint, obtained by multiplying a series of timelike and spacelike joints together with ordinary CSs.

is a primal (dual)  $c$ -colored correlation surface, referred to as a “p(d)c-CS.”

It is straightforward to see that, for a spacelike or timelike face  $f$ ,  $S_{\text{CS}}(f)$  is an A- or L-type SG around the AQ or link corresponding to  $f$ , respectively. The following theorem relates general 2-chains to stabilizers of the CCCS.

**Theorem 1 (CSs as stabilizers).** *For a 2-chain  $h_2$ ,  $S_{\text{CS}}(h_2)$  is a stabilizer if and only if  $Q(h_2) \cap Q_{\text{IN}} = \emptyset$ , where  $Q_{\text{IN}}$  is the set of input qubits defined in Sec. II which are not initialized to the  $|+\rangle$  states.*

*Proof. (If part)* Since qubits outside  $Q_{\text{IN}}$  is initialized to the  $|+\rangle$  states, there exist the A- or C-type SG around each of them, as discussed in Sec. II. Let  $F := \{f \in \mathcal{B}_2^{\text{pc}} \mid Q(f) \cap Q_{\text{IN}} = \emptyset\}$  be a set of faces. For a face  $f \in F$ ,  $S_{\text{CS}}(f)$  is a stabilizer; it is an A- or L-type SG. For a 2-chain  $h_2 \in H_2^{\text{pc}}$  where  $Q(h_2) \cap Q_{\text{IN}} = \emptyset$ ,  $h_2$  can be written as a linear summation of elements in  $F$ :  $\exists \{f_i\} \subseteq F$ ,  $h_2 = \sum_i f_i$ . Since the map  $\partial$  is linear and  $P(h)P(h') = P(h + h')$  holds for any Pauli operator  $P$ ,  $S_{\text{CS}}(h_2) = X(h_2)Z(\partial h_2) = \prod_i X(f_i)Z(\partial f_i) = \prod_i S_{\text{CS}}(f_i)$ , which is a stabilizer. The proof is analogous for dual 2-chains.

*(Only if part)* Since qubits in  $Q_{\text{IN}}$  are not initialized to the  $|+\rangle$  states, the A- and C-type SGs around each of them do not exist. Therefore, the  $X$ -support of any stabilizer cannot contain qubits in  $Q_{\text{IN}}$ .  $\square$

Regarding a primal CS  $S := S_{\text{CS}}(h_2)$ ,  $Q(h_2)$  is called the *interior* of  $S$ , in which every qubit is primal and in  $\text{supp}_X(S)$ . Similarly,  $Q(\partial h_2)$  is called the *boundary* of  $S$ , in which every qubit is dual and in  $\text{supp}_Z(S)$ . We say

that  $S$  is *timelike* (*spacelike*) if  $h_2$  is composed of timelike (spacelike) faces only.

CSs discussed above include all A- and L-type SGs, but not J-type SGs in Fig. 5(d). Each J-type SG can be regarded as three primal timelike CSs with different colors “joined” along a timelike series of CQs as Fig. 7(a), in the sense that each “wing” of a color  $c$  may be extended by multiplying ordinary pc-CSs. Note that the CQs along the joint are not included in the support.

A question arising naturally may be about “spacelike” joints, and those are also possible as presented in Fig. 7(b). A timelike pc-CS and two spacelike primal CSs with the other two colors may be joined along a spacelike series of pcLs. Such a joint can be obtained by multiplying several A-type SGs along a spacelike boundary of the timelike CS. Note that the ends of spacelike and timelike joints may fit perfectly with each other, in the sense that all the  $Z$  operators on the joint cancel out when multiplying them.

A general joint of CSs with different colors can be obtained as Fig. 7(c) by multiplying several spacelike and timelike joints together with ordinary CSs. We refer to such a primal CS with a joint as a “pj-CS.” For consistency with ordinary CSs, we define the *interior* (*boundary*) of a pj-CS by its  $X$  ( $Z$ )-support, which is intuitive considering its visualization in Fig. 7.

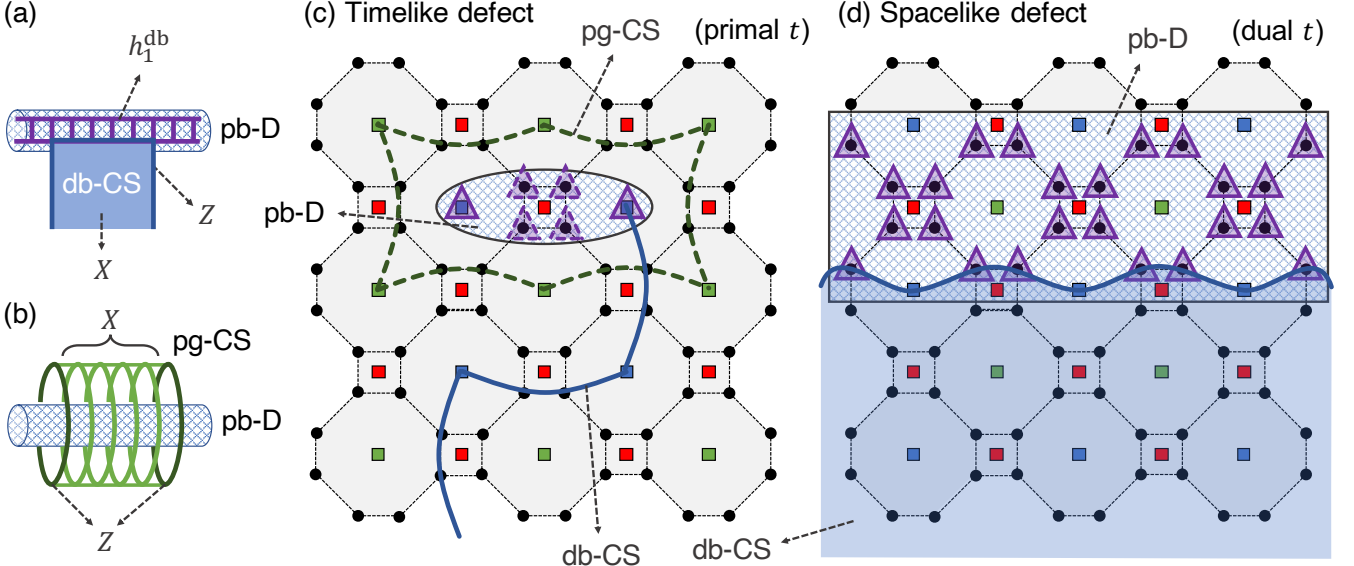


FIG. 8. (a) Schematic diagram of a defect (pb-D) and a db-CS  $S$  ending at the defect. The cylinder indicates the defect area and the purple lines indicate the defect, a 1-chain  $h_1^{\text{db}} \in H_1^{\text{db}}$ . Qubits corresponding to  $h_1^{\text{db}}$  are measured in the  $Z$  basis. (b) Schematic diagram of a pg-CS surrounding a pb-D. (c) A primal layer in a 8-8-4 CCCS penetrated by a timelike pb-D. The cross section of the defect area is displayed as a checkered pattern. Each purple triangle with a solid (dashed) border indicates a defect pbAQ (pCQ) in the layer (next layer) measured in the  $Z$  basis. The cross sections of a timelike db-CS ending at the defect and a timelike pg-CS surrounding it are presented as a blue solid line and a green dashed line, respectively. The solid (or dashed) lines indicate faces bisected by the layer (or ending at the layer). That is, the corresponding qubits are on the layer (or an adjacent layer). (d) A dual layer in a 8-8-4 CCCS containing a spacelike pb-D. The defect area is displayed as a checkered pattern. A db-CS ending at the defect is visualized as a blue surface, where the blue line corresponds to its boundary.

#### IV. MEASUREMENT-BASED QUANTUM COMPUTATION VIA COLOR-CODE-BASED CLUSTER STATES

In this section, we describe MBQC via CCCSs. We first introduce defects and define qubits using them. We then construct basic logical gates including the identity, CNOT, Hadamard, phase, and  $T$  gates, which together constitute a universal set of gates, through CSs defined in the previous section.

As mentioned in Sec. II, each qubit except the output qubits ( $Q_{\text{OUT}}$ ) is measured in a Pauli basis determined by a predefined measurement pattern. Such a qubit is included in an area with one of the four types: *vacuum*, *defect*, *Y-plane*, and *injection qubit*. There may be multiple defects, Y-planes, and injection qubits, and the entire remaining area is the vacuum. Defects are key ingredients for the protocol; all the logical operations completely depend on how to place them. Y-planes are used in fault-tolerant  $Y$ -measurements on physical qubits for the logical Hadamard and phase gates. Lastly, each injection qubit is a special area for state injection and consists of a single qubit. Qubits in each area are measured as follows:

#### Measurement pattern

$$\text{A qubit is measured in the basis of } \begin{cases} X & \text{if in the vacuum or an injection qubit,} \\ Z & \text{if in a defect,} \\ Y & \text{if in a Y-plane.} \end{cases} \quad (3)$$

Arranging these elements besides the vacuum properly is the key for implementing logical qubits and gates, which is what we cover in this section.

#### A. Defects and related correlation surfaces

Defects are defined as follows and visualized in Fig. 8(a) schematically.

**Definition 5 (Defect).** Consider a stick-shaped area in the space called a defect area. A primal (dual) c-colored defect, referred to as a “ $p(d)c$ -D,” is a 1-chain  $h_1 \in H_1^{d(p)c}$  such that  $Q(h_1)$  contains all the  $p(d)c$ AQs and  $p(d)c$ CQs in the defect area. Qubits in  $Q(h_1)$  are called defect qubits and measured in the  $Z$  basis during the measurement step.

We say that a defect is *timelike* or *spacelike* if the defect area stretches timelike or spacelike, respectively. Figure 8(c) and (d) illustrate the explicit structures of

timelike and spacelike defects, respectively, in an 8-8-4 CCCS.

After the measurement step, only CSs commuting with the measurement pattern survive. The following theorem gives the conditions which such CSs satisfy.

**Theorem 2 (Compatible CSs).** *Considering only the vacuum and defects, a CS  $S$  is “compatible,” or still a stabilizer after the measurement step, if and only if the followings hold:*

$$Q_{\text{int}}(S) \setminus Q_{\text{OUT}} \subseteq V \setminus Q_{\text{IN}}, \quad (4a)$$

$$Q_{\text{bnd}}(S) \setminus Q_{\text{OUT}} \subseteq D, \quad (4b)$$

where  $Q_{\text{int(bnd)}}(S)$  is the interior (boundary) of  $S$ ,  $Q_{\text{IN(OUT)}}$  is the set of input (output) qubits defined in Sec. II, and  $V$  ( $D$ ) is the set of all vacuum (defect) qubits.

We particularly want to emphasize that a compatible CS cannot end in the vacuum. Note that  $Q_{\text{IN}}$  is excluded in the right-hand side (RHS) of Eq. (4a) due to Theorem 1.

Table II shows allowed positional relations between a pc-D  $d$  and a compatible CS with each primality and color, derived from Theorem 2 and Table I. Remark that  $d$  is composed of pcAQs and pcCQs. A pc'-CS has primal interior qubits which should be measured in the  $X$  basis for the CS to be compatible, thus can overlap with  $d$  unless they share common qubits, which is possible only if  $c' = c$  and the overlapped region of the CS is spacelike.<sup>3</sup> Since its boundary qubits are dual, it cannot end at  $d$ . A dc'-CS has primal boundary qubits, thus can end at  $d$  if the boundary qubits are in  $d$ , which is possible if  $c' = c$ .<sup>4</sup> Since its interior qubits are dual, it can freely pass  $d$ .

We mainly concern two types of CSs with respect to a pc-D: pc-CSs surrounding the defect and dc-CSs ending at it, as shown schematically in Fig. 8(a) and (b) and explicitly in Fig. 8(c) and (d). Each of such CSs is compatible except for the two ends with respect to the direction of the defect.

TABLE II. Allowed positional relations between a primal defect  $d$  and a compatible CS. The relations for dual defects are analogous.

With a pc-D $d$ , a <b>xy</b> -CS $S$ ...		
$\begin{array}{c} y \\ \diagup \\ x \end{array}$	$c$	$c' (\neq c)$
p	can overlap with $d$ only if $S$ is spacelike	cannot overlap with $d$
d	can end at $d$	cannot end at $d$

<sup>3</sup> If this is the case, the interior qubits of the CS correspond to spacelike faces in  $\mathcal{L}^{\text{pc}}$ , which are pc''AQs ( $c'' \neq c$ ) according to Table I. They are surely not be in the pc-D. Otherwise, the pc'-CS and defect share at least one qubit if they overlap.

<sup>4</sup> The boundary qubits of a dc-CS correspond to edges in  $\mathcal{L}^{\text{dc}}$ , which are pcAQs or pcLs.

## B. Defining a logical qubit

We first define *connected* 1-chains as follows.

**Definition 6 (Connected 1-chain).** *A 1-chain  $h_1$  is connected if and only if it satisfies  $|\partial h_1| \leq 2$ . It is regarded to be closed if  $|\partial h_1| = 0$  and open otherwise.*

To define a logical qubit, we consider three parallel timelike defects with different colors passing through the layer of  $t = t_0$  for a given integer  $t_0$ , as visualized schematically in Fig. 9(a). We assume that the qubits with  $t = t_0$  are the input qubits ( $Q_{\text{IN}}$ ) and all the qubits with  $t < t_0$  have already been measured. The constructed logical qubit is primal (dual) if the defects are primal (dual) and  $t_0$  is odd (even).

We first define the logical- $X$  ( $X_L$ ) operator of a primal logical qubit. For a given pair of different colors  $(c, c')$ , we consider two closed connected spacelike 1-chains, as shown in Fig. 9(a) for  $(c, c') = (\text{b}, \text{r})$ . The first one is  $h_1^{X_{\text{dcc}'}} \in H_1^{\text{dc}}$  located in the layer of  $t = t_0$  and surrounding the pc'-D. The second one is  $h_1^{X_{\text{pcc}'}} \in H_1^{\text{pc}}$  defined by parallelly moving  $h_1^{X_{\text{dcc}'}}$  one unit positively along the time axis. Note that the two 1-chains consist of pcLs and dcLs, respectively. We then define

$$X_L := F_X^{cc'}(t_0) := X(h_1^{X_{\text{dcc}'}}) Z(h_1^{X_{\text{pcc}'}}). \quad (5)$$

Note that a pc-CS may end at  $\text{supp}_Z(X_L) = Q(h_1^{X_{\text{pcc}'}})$ , since its boundary is also a 1-chain in  $H_1^{\text{pc}}$ . The colors  $c$  and  $c'$  can be any pair of different colors, and they are proven to be equivalent in Sec. IV D 2.

For the logical- $Z$  ( $Z_L$ ) operator of a primal qubit, we consider an open connected spacelike 1-chain  $h_1^{Z_c} \in H_1^{\text{dc}}$  for each color  $c$ , which is located in the layer of  $t = t_0$  and connects the pc-D and a common pcCQ  $q_I$ , as shown in Fig. 9(a) and (b). Note that  $h_1^{Z_c}$  is composed of pcLs. We define

$$\begin{aligned} Z_L &:= F_Z(t_0) \\ &:= Z(h_1^{Z_r}) Z(h_1^{Z_g}) Z(h_1^{Z_b}) Z(q_I). \end{aligned} \quad (6)$$

Note that  $q_I$  is out of  $\text{supp}(Z_L)$ . It is worth noticing that a dj-CS may end at  $\text{supp}(Z_L)$ , since the “Y”-shaped boundary of the CS shown in Fig. 7(c) may be completely in  $\text{supp}(Z_L)$ .

$X_L$  and  $Z_L$  defined above anticommute with each other, considering that  $\text{supp}_Z(Z_L)$  and  $\text{supp}_X(X_L)$  meet at a pcCQ  $q_{\text{anti}}$  in Fig. 9(a). A dual logical qubit is defined analogously, but now the logical operators are defined oppositely;  $\text{supp}(Z_L)$  surrounds a defect and  $\text{supp}(X_L)$  ends at each defect.

## C. Initialization and measurement of a logical qubit

The  $X_L$ -initialization of a primal logical qubit is done by making the defects start from the layer of  $t = t_0$  and

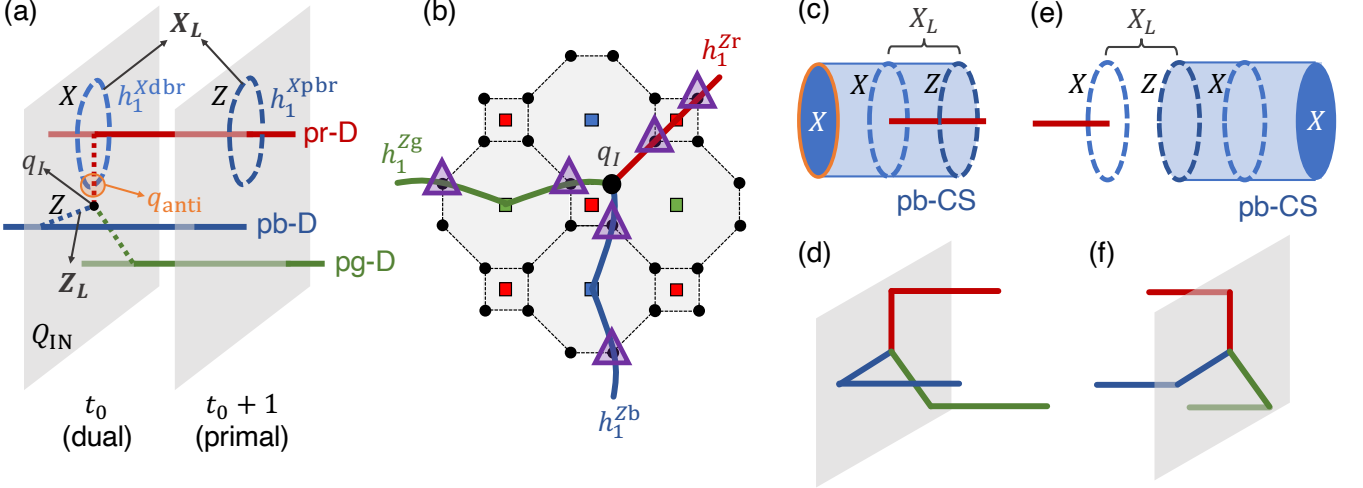


FIG. 9. Definition of a primal logical qubit and its initialization and measurement. (a) Schematic diagram of a primal logical qubit composed of three parallel primal timelike defects with different colors. Qubits in the dual layer of  $t = t_0$  are regarded as the input qubits ( $Q_{IN}$ ). Blue dashed lines indicate 1-chains  $h_1^{xdbr}$  and  $h_1^{xpbr}$ , which constitute  $\text{supp}_X(X_L)$  and  $\text{supp}_Z(X_L)$ , respectively. Red, green, and blue dotted lines indicate 1-chains  $h_1^{Zr}$ ,  $h_1^{Zg}$ , and  $h_1^{Zb}$ , respectively, which constitute  $\text{supp}_Z(Z_L)$  except the pCQ  $q_I$  at which they end.  $\text{supp}_X(X_L)$  and  $\text{supp}_Z(Z_L)$  meet at a pCQ  $q_{anti}$ , thus they anticommute with each other. (b) Structure of  $Z_L$  near  $q_I$  in a 8-8-4 CCCS. Colored lines are  $h_1^{Zr}$ ,  $h_1^{Zg}$ , and  $h_1^{Zb}$ , respectively. Purple triangles indicate  $\text{supp}(Z_L)$ . (c)  $X_L$ -initialization of a primal logical qubit is done by making the defects start from  $t = t_0$  and excluding the qubits with  $t = t_0$  from  $Q_{IN}$ .  $X_L$  is then a part of a pb-CS. It is initialized to  $|\pm_L\rangle$  depending on the  $X$ -measurement results of the faces marked as a blue circle with an orange boundary. (d)  $Z_L$ -initialization of a primal logical qubit is done by extending the defects spatially along  $\text{supp}(Z_L)$  and excluding the qubits with  $t = t_0$  from  $Q_{IN}$ . It is initialized to  $|0_L\rangle$  or  $|1_L\rangle$  depending on the  $Z$ -measurement results of the extended defects. (e)  $X_L$ - and (f)  $Z_L$ -measurement. Each of them is done by reversing the corresponding initialization process. The  $X_L$ -measurement is done using a pb-CS  $S_{CS}(h_2)$  where  $Q(\partial h_2) = \text{supp}_Z(X_L)$ . The  $Z_L$ -measurement is done by extending each defect along  $\text{supp}(Z_L)$ .

excluding the qubits with  $t = t_0$  from  $Q_{IN}$ .  $X_L$  given in Eq. (5) is then a part of a “cup-shaped” compatible primal CS  $S$  as shown in Fig. 9(c):  $S = X_L \prod_i X_i$ , where  $X_i$ ’s are the  $X$  operators on some qubits with  $t = t_0 - 1$ . The logical qubit is therefore initialized to  $|\pm_L\rangle$  depending on the measurement result of  $\prod_i X_i$ .

The  $Z_L$ -initialization of a primal logical qubit is done by making the defects start from the layer of  $t = t_0$  and extending them spatially along  $\text{supp}(Z_L)$ , as shown in Fig. 9(d). The logical qubit is then initialized to  $|0_L\rangle$  or  $|1_L\rangle$  depending on the  $Z$ -measurement results of the qubits in  $\text{supp}(Z_L)$ .

The  $X_L$ - or  $Z_L$ -measurement procedure is done just by reversing the time order from the corresponding initialization process, as shown in Fig. 9(e) and (f). The measurement result is determined by the single-qubit measurement results.

#### D. Elementary logical gates

Now we describe the implementation schemes of the elementary logical gates. We first construct the identity gate and present general principles for building up logical gates. We then consider the CNOT, Hadamard, and phase gates which together completely generate the

Clifford group.

##### 1. Identity gate

The identity gate of a primal logical qubit is constructed just by extending the defects of the logical qubit along the time axis from  $t = t_0$  to  $t = t_1$  as Fig. 10. Let  $X_L$  and  $X'_L$  be the logical- $X$  operators on the input and output layers respectively, namely,  $X_L := F_X^{\text{br}}(t_0)$  and  $X'_L := F_X^{\text{br}}(t_1)$  where  $F_X^{\text{br}}(\cdot)$  is given in Eq. (5). We consider a pb-CS  $S_X$  which surrounds the pr-D and ends at  $\text{supp}_Z(X_L)$  and  $\text{supp}_Z(X'_L)$ , as shown in Fig. 10(a). Since  $S_X$  is a stabilizer,  $X_L$  may be redefined by multiplying  $S_X$ :  $\tilde{X}_L := S_X X_L$ . The following then holds:

$$\tilde{X}_L = \left( \bigotimes_{q \in V_X} X(q) \right) X'_L, \quad (7)$$

where  $V_X := \text{supp}_X(X_L) \cup Q_{\text{int}}(S_X) \setminus \text{supp}_X(X'_L) \subset V$ . After the measurements of qubits with  $t < t_1$ , the RHS of the above equation is transformed into  $x_X X'_L$  for  $x_X := \prod_{q \in V_X} x_q \in \{\pm 1\}$ , where  $x_q$  ( $z_q$ ) is the  $X$  ( $Z$ )-measurement result of the qubit  $q$ .

We do a similar thing on the  $Z_L$  operators. Denoting those at the input and output layers as  $Z_L$  and  $Z'_L$  re-

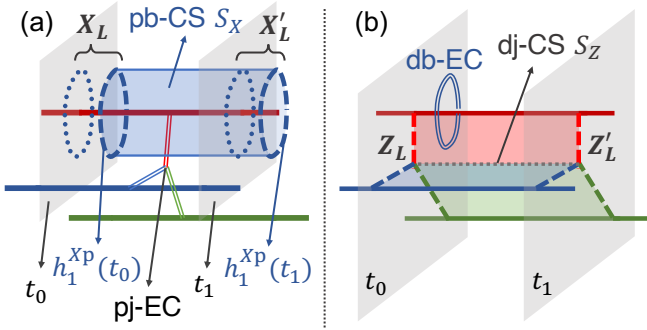


FIG. 10. Logical identity gate of a primal logical qubit constructed by extending the defects of the qubits from  $t = t_0$  to  $t = t_1$ . The logical- $X$  operator on the layer of  $t = t_0$  ( $t_1$ ) is  $X_L$  ( $X'_L$ ), and  $Z_L$  and  $Z'_L$  are defined similarly. (a)  $X_L$  is transformed into  $X'_L$  via a pb-CS  $S_X$  surrounding the red defect, and (b)  $Z_L$  is transformed into  $Z'_L$  via a dj-CS  $S_Z$  ending at the three defects.  $h_1^{X_p}(\cdot)$  in (a) is  $h_1^{X_{p\text{br}}}(\cdot)$  defined in Sec. IV B. Double lines indicate error chains causing logical errors covered in Sec. V A.

spectively, we consider a dj-CS  $S_Z$  ending at  $\text{supp}(Z_L)$ ,  $\text{supp}(Z'_L)$ , and the defects, as Fig. 10(b). Redefining  $Z_L$  as  $\tilde{Z}_L := S_Z Z_L$ , the following holds

$$\tilde{Z}_L = \left( \bigotimes_{q \in V_Z} X(q) \right) \left( \bigotimes_{q \in D_Z} Z(q) \right) Z'_L,$$

where  $V_Z := Q_{\text{int}}(S_Z) \subset V$  and  $D_Z := Q_{\text{bdr}}(S_Z) \setminus \text{supp}(Z_L Z'_L) \subseteq D$ . After the measurements of qubits with  $t < t_1$ , the RHS transforms into  $x_Z z_Z Z'_L$  where  $x_Z := \prod_{q \in V_Z} x_q$  and  $z_Z := \prod_{q \in D_Z} z_q$ .

The transformation of the logical operators is summarized as

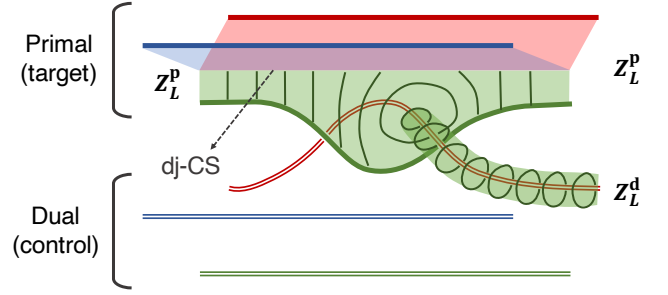
$$X_L \rightarrow x_X X'_L, \quad Z_L \rightarrow x_Z z_Z Z'_L, \quad (8)$$

which is the Heisenberg's picture of the process. In terms of the Schrödinger's picture, the initial logical state  $|\psi_L\rangle$  is transformed as

$$|\psi_L\rangle \rightarrow |\psi'_L\rangle = X_L^{(1-x_Z z_Z)/2} Z_L^{(1-x_X)/2} |\psi_L\rangle,$$

which corresponds to the identity gate up to some byproduct operators determined by the measurement results. The byproduct operators can be handled by a software to be delayed to the end of the entire circuit, and finally merged with the logical measurements [24].

The above arguments show the basic ideas for implementing logical gates. Regarding  $n$  logical qubits, let  $P_{Li}$  for each  $P \in \{X, Z\}$  and integer  $i \leq n$  denote the logical- $P$  operator of the  $i$ th logical qubit. To construct a general logical gate  $U$  for  $n$  logical qubits, one should find a configuration of defects (and Y-planes for some gates) where a CS  $S_{Pi}$  exists for each  $P_{Li}$  satisfying the following conditions:



**Condition 1.**  $S_{Pi}$  should connect  $P_{Li}$  on the input layer and  $U^\dagger P_{Li} U$  on the output layer.  $X_L$  ( $Z_L$ ) of a primal logical qubit can be connected with a p(d)-CS, and vice versa for a dual logical qubit

**Condition 2.**  $S_{Pi}$  should be compatible with the measurements on the qubits between the initial and final layers; it satisfies the relationships shown in Table II.

If such CSs exist, the configuration implements the desired logical gate with some byproduct operators obtained from the measurement results.

## 2. CNOT and primality-switching gates

We first consider the logical CNOT gate between a primal logical qubit (target) and a dual one (control). Figure 11 illustrates the defect configuration, where the pg-D of the primal logical qubit and the dr-D of the dual one are twisted one round with each other. The logical Pauli operators are transformed as

$$X_L^p I_L^d \rightarrow X_L^p I_L^d, \quad I_L^p X_L^d \rightarrow X_L^p X_L^d, \\ Z_L^p I_L^d \rightarrow Z_L^p Z_L^d, \quad I_L^p Z_L^d \rightarrow I_L^p Z_L^d, \quad (9)$$

where the tensor product symbols and the sign terms such as  $x_X$ ,  $x_Z$ , and  $z_Z$  in Eq. (8) are omitted, and each superscript p or d indicates the primality of the logical qubit. The above transformation is exactly the Heisenberg picture of the CNOT gate where the primal logical qubit is the target.

We need to find CSs satisfying two Conditions presented in Sec. IV D 1 to verify the transformations in Eq. (9). A dual CS for the transformation of  $Z_L^p \otimes I_L^d$  is presented schematically in Fig. 11. Note that the “tunnel” of the CS along the dr-D must be formed since the dr-D cannot overlap with a dg-CS (see Table II). A CS for  $I_L^p \otimes X_L^d$  can be constructed analogously; now, a tunnel of a pr-CS is made along the pg-D. The other two transformations are straightforward.

Exploiting the CNOT gate discussed above, it is possible to make the *primality-switching* gate which changes a

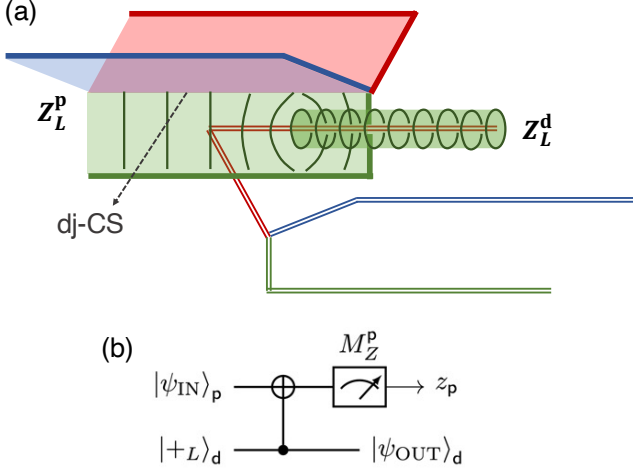


FIG. 12. (a) Construction of the primality-switching gate changing a primal logical qubit to a dual one.  $Z_L^p$  is transformed into  $Z_L^d$  via the presented dj-CS. (b) Circuit equivalent to the primality-switching gate.  $M_Z^p$  is the  $Z_L$ -measurement on the primal qubit, and the result is  $z_p$ .

primal logical qubit to a dual one, by “closing” the input part of the dual one and the output part of the primal one, as shown in Fig. 12(a). Remark that these closures indicate the  $Z_L$ -measurement of the primal one and the  $X_L$ -initialization of the dual one. The modified configuration is thus equivalent to the circuit in Fig. 12(b) up to byproduct operators. The logical operators are transformed along the circuit as:

$$\begin{array}{lcl} X_L^p I_L^d & \xrightarrow{\text{CNOT}} & I_L^p X_L^d \xrightarrow{M_Z^p} X_L^d, \\ Z_L^p I_L^d & \xrightarrow{\quad} & Z_L^p Z_L^d \xrightarrow{\quad} z_p Z_L^d, \end{array}$$

where the equivalence relation (“ $\sim$ ”) is from multiplying the initial stabilizer  $I_L^p X_L^d$ . The circuit thus implement the identity gate up to byproduct products, while changing the primality. Alternatively, this result is directly obtainable by finding appropriate CSs; for example, the dj-CS in Fig. 12(a) verify the transformation of  $Z_L^p$  to  $Z_L^d$ . The primality-switching gate from a dual logical qubit to a primal one can be made in a similar manner.

The primality-switching gate enables the CNOT gate between logical qubits with arbitrary primalities. Regardless of the primalities of the initial logical qubits, one can switch them to primal (target) or dual (control), and apply the CNOT gate in Fig. 11.

Note that the equivalence between the different definitions of the  $X_L$  operator, related to the choice of the color pair  $(c, c')$  in Eq. (5), can be proven with the primality-switching gate. We consider a chain of two primality-switching gates: primal  $\rightarrow$  dual  $\rightarrow$  primal. No matter how  $X_L$  is defined in the first primal logical qubit, it becomes symmetric about the color in the dual one. We can thus transform it into any definition of  $X_L$  in the final primal one.

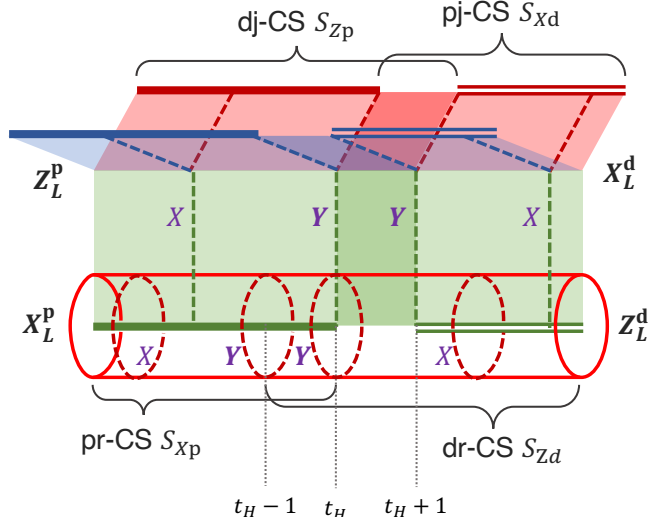


FIG. 13. Construction of the Hadamard gate from a primal logical qubit to a dual one. Each colored single (double) line is the primal (dual) defect of that color. The presented d(p)j-CS  $S_{Zp}$  ( $S_{Xd}$ ) ends at the three primal (dual) defects and the layer of  $t = t_H + 1$  ( $t = t_H$ ). The presented p(d)r-CS  $S_{Xp}$  ( $S_{Zd}$ ) surrounds the p(d)g-D and ends at the layer of  $t = t_H$  ( $t = t_H - 1$ ).  $S_{ZX} := S_{Zp}S_{Xp}$  and  $S_{XZ} := S_{Xp}S_{Zd}$  transform the logical Pauli operators as Eq. (10). The supports of  $S_{ZX}$  and  $S_{XZ}$  are marked as colored dashed lines. For the  $Y$ -measurements to be fault-tolerant, a dual Y-plane is placed on  $t = t_H$  and primal Y-planes are placed on  $t = t_H - 1$  and  $t_H + 1$ .

### 3. Hadamard gate

To construct the logical Hadamard gate, the logical Pauli operators should be transformed as

$$X_L \rightarrow Z_L, \quad Z_L \rightarrow X_L. \quad (10)$$

It is simple if the gate is located just after the state injection presented in the next subsection: injecting the unencoded state to a dual logical qubit instead of a primal one. This method is valid since the definitions of  $X_L$  and  $Z_L$  are opposite for primal and dual logical qubits.

If the Hadamard gate is located in the middle of the circuit, it is a bit tricky. Since  $X_L$  ( $Z_L$ ) of a primal qubit can be connected only with p(d)-CSs, there should be a CS which is primal near the initial layer but dual near the output layer, to achieve the transformation. To solve this problem, we construct a defect structure starting with a primal logical qubit and ending with a dual one as shown in Fig. 13, where the primal one stops at the primal layer of  $t = t_H$  and the dual one starts from the dual layer of  $t = t_H + 1$ . Each pair of defects with the same color must have exactly the same spatial structure at  $t = t_H$  and  $t = t_H + 1$ . Note that such a configuration is possible thanks to the self-duality of the 2D color codes which makes primal and dual layers have exactly the same structure.

We consider two pairs of overlapping primal and dual

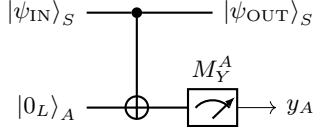


FIG. 14. Circuit for the logical phase gate of a system logical qubit ( $S$ ) with an ancilla logical qubit ( $A$ ).  $M_Y^A$  is the  $Y_L$ -measurement on the ancilla qubit with the result of  $y_A$ .

CSs:  $(S_{Zp}, S_{Xd})$  and  $(S_{Xp}, S_{Zd})$ , where  $S_{Xp}$ ,  $S_{Zp}$ ,  $S_{Xd}$ , and  $S_{Zd}$  are a pr-CS, dj-CS, pj-CS, and dr-CS defined in Fig. 13, respectively.  $S_{ZX} := S_{Zp}S_{Xd}$  then transforms  $Z_L$  of the initial primal logical qubit to  $X_L$  of the final dual one. Similarly,  $S_{XZ} := S_{Xp}S_{Zd}$  transforms the initial  $X_L$  to the final  $Z_L$ . Condition 1 in Sec. IV D 1 is thus satisfied with these two “hybrid” CSs. What remains is Condition 2. Since  $S_{ZX}$  and  $S_{XZ}$  contain  $Y$  operators on some CQs in the overlapping regions, the qubits should be measured in the  $Y$  basis for the CSs to be compatible.

To make the  $Y$ -measurements fault-tolerant, we introduce  $Y$ -planes:

**Definition 7 (Y-plane).** A primal (dual) Y-plane is the set of p(d)CQs in an area contained in a dual (primal) layer. CQs in Y-planes are measured in the  $Y$  basis.

Errors in Y-planes can be corrected by an error correction procedure presented in Sec. IV A. Therefore, the  $Y$ -measurements for the Hadamard gate can be fault-tolerantly done by placing wide enough Y-planes to cover  $\text{supp}_Y(S_{ZX})$  and  $\text{supp}_Y(S_{XZ})$  completely.

#### 4. Phase gate

We now complete the generating set of the Clifford group with the construction of the logical phase gate. The desired transformation for it is

$$X_L \rightarrow -Y_L, \quad Z_L \rightarrow Z_L, \quad (11)$$

which can be achieved via the circuit in Fig. 14 with an ancilla logical qubit initialized to the  $|0_L\rangle$  state. To check this, we simply need to follow the transformation of the logical operators:

$$\begin{array}{ccccc} X_L^S I_L^A \sim X_L^S Z_L^A & \xrightarrow{\text{CNOT}} & -Y_L^S Y_L^A & \xrightarrow{M_Y^A} & -y_A Y_L^S, \\ Z_L^S I_L^A & \xrightarrow{\quad} & Z_L^S I_L^A & \xrightarrow{\quad} & Z_L^S, \end{array}$$

where  $P_L^{S(A)}$  for  $P \in \{I, X, Y, Z\}$  denotes the logical- $P$  operator of the system (ancilla) logical qubit, and the equivalence relation (“ $\sim$ ”) is from multiplying the initial stabilizer  $I_L^S Z_L^A$ . The circuit thus implement the phase gate up to a byproduct operator determined by  $y_A$ .

All the elements in the circuit already have been described except the  $Y_L$ -measurement. For the  $Y_L$ -measurement of a primal logical qubit, we simply extend

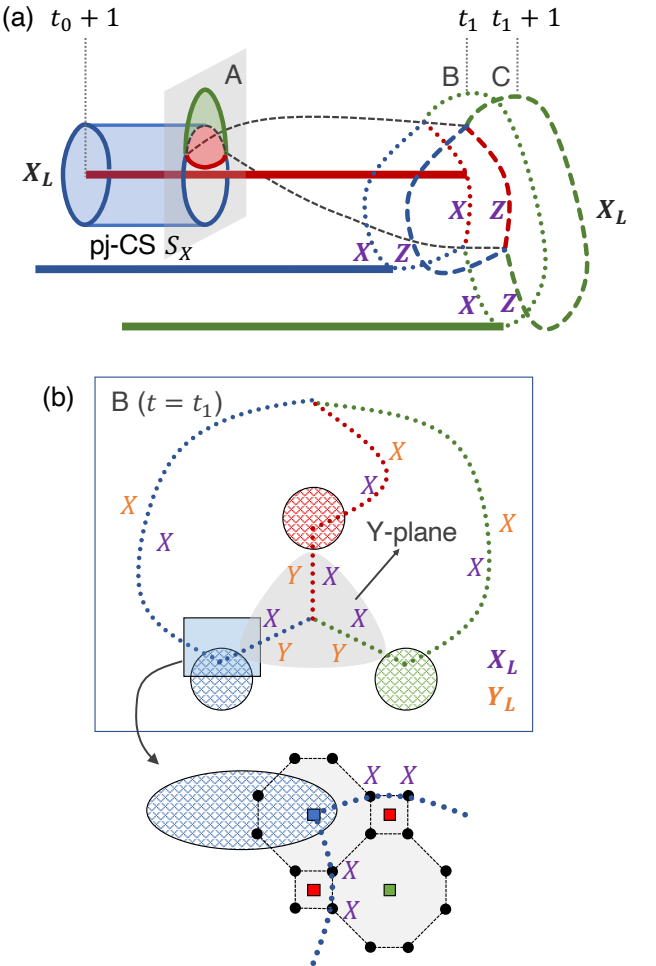


FIG. 15. (a) pj-CS  $S_X$  for the  $Y_L$ -measurement of a primal logical qubit.  $S_X$  initially has the form of a pb-CS surrounding the pr-D. On layer A, it is divided into three primal CSs with different colors through a spacelike joint. Each CS is then deformed appropriately so that the joint is extended along the black dashed line.  $S_X$  ends at the layer C of  $t = t_1 + 1$ . On layer C,  $S_X$  has the  $Z$ -support along the connected 1-chains marked as dashed lines. On the layer B of  $t = t_1$ ,  $S_X$  has the  $X$ -support along the connected 1-chains marked as dotted lines.  $X_L$  transformed via  $S_X$  contains the  $X$  and  $Z$  operators on the layer B and C. (b) Structure of layer B. The supports of the transformed  $X_L$  and  $Y_L$  operators are marked as dotted lines with the corresponding Pauli operators. The  $Y$ -support qubits of  $Y_L$  are covered by a Y-plane to make the  $Y$ -measurements fault-tolerant. The junction of the pb-D and the corresponding connected 1-chain is explicitly shown below.

the defects along the time axis from  $t = t_0$  to  $t = t_1$  such as the logical identity gate in Fig. 10. The initial  $Z_L$  transformed into the final  $Z_L$  via  $S_Z$  defined in Fig. 10(b). However, we define a different  $S_X$  by a pj-CS illustrated in Fig. 15(a), instead of a pb-CS surrounding the pr-D as in Fig. 10(a).  $S_X$  is constructed such that the  $X$ -support of the transformed  $X_L$  contains the  $Z$ -support of the transformed  $Z_L$ , which is a “Y”-shape

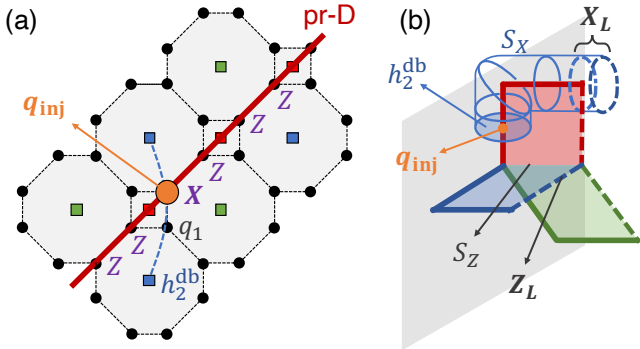


FIG. 16. State injection procedure. (a) An unencoded state is injected into an injection qubit  $q_{\text{inj}}$  in the pr-D which is spacelike and thicknessless at  $q_{\text{inj}}$ .  $Z(q_{\text{inj}})$  is invariant when the CZ gates associated with  $q_{\text{inj}}$  are applied. However,  $X(q_{\text{inj}})$  is transformed into  $S(q_{\text{inj}})$ , where  $S(q_{\text{inj}})$  is the C-type SG around  $q_{\text{inj}}$ . Note that  $S(q_{\text{inj}})$  is not a stabilizer since  $q_{\text{inj}}$  is not initialized to  $|+\rangle$ .  $S(q_{\text{inj}})$  is equivalent to  $S_{\text{CS}}(h_2^{\text{db}})$  since  $S_{\text{CS}}(h_2^{\text{db}}) = S(q_{\text{inj}})S(q_1)$ , where  $h_2^{\text{db}} \in H_2^{\text{db}}$  is the timelike 2-chain marked as a blue dashed line and  $q_1$  is the marked CQ adjacent to  $q_{\text{inj}}$ .  $q_{\text{inj}}$  is measured in the  $X$  basis during the measurement step. (b)  $S_{\text{CS}}(h_2^{\text{db}})$  is transformed into  $X_L$  via the pb-CS  $S_X$ .  $Z(q_{\text{inj}})$  is transformed into  $Z_L$  via the dj-CS  $S_Z$ .

series of pCQs connecting the three defects. The transformed  $Y_L$  ( $= iX_L Z_L$ ) thus has the  $Y$ -support along the “Y”-shape as shown in Fig. 15(b), which can be fault-tolerantly measured by placing a Y-plane between the three defects. The remained  $Z$  operators in the transformed  $Y_L$  are transformed back to the  $Z$  operators along a closed connected blue 1-chain around the pr-D through the process opposite to the process so far, then measured via a process similar to the  $X_L$ -measurement in Fig. 9.

We conclude that all the elements in the circuit of Fig. 14 can be implemented fault-tolerantly, thus the fault-tolerant phase gate can be made up to byproduct operators.

## E. State injection

Preparation of an arbitrary logical qubit  $a|0_L\rangle + b|1_L\rangle$  is essential for implementing the logical  $T$  gate as well as quantum computation with arbitrary input states. This is done in our scheme by injecting the corresponding un-encoded state into a physical qubit.

We start from the configuration for the  $Z_L$ -initialization of a primal logical qubit shown in Fig. 9(c), where three defects meet at a point. First, a qubit  $q_{\text{inj}}$  in the pc-D for any color  $c$  is selected as an *injection qubit*. We assume that the defect is “thicknessless” at  $q_{\text{inj}}$ ; namely, its cross section at  $q_{\text{inj}}$  contains at most one qubit as shown in Fig. 16(a). The desired initial state is injected into  $q_{\text{inj}}$  in an unencoded form  $|\psi\rangle = a|0\rangle + b|1\rangle$ , then the associated CZ gates are applied. Remark that

$q_{\text{inj}}$  is measured in the  $X$  basis as stated in Eq. (3). The  $X$  ( $Z$ ) operator on  $q_{\text{inj}}$  is transformed into  $X_L$  ( $Z_L$ ) up to a sign factor as shown in Fig. 16, thus the logical state  $|\psi_L\rangle = a|0_L\rangle + b|1_L\rangle$  is prepared up to byproduct operators.

Note that the state injection procedure is inherently not fault-tolerant, since it uses an unprotected single-qubit state and the defect is thicknessless at  $q_{\text{inj}}$ . Therefore, magic state distillation is essential for the faithful  $T$  gate.

## V. ERROR CORRECTION

Now we describe error correction schemes in CCCSs. The scheme varies with the area of the qubits: the vacuum, defects, and Y-planes.

### A. Error correction in the vacuum and defects

For error correction in the vacuum, we exploit *parity-check operators* (PCs) defined as follows:

**Definition 8 (Parity-check operator).** For each cell  $c$ , the CS

$$S_{\text{CS}}(\partial c) = X(\partial c)$$

is a parity-check operator (PC), where  $S_{CS}(\cdot)$  is given in Eq. (2).

PCs are classified into six groups according to primalities and cell colors. Here, the primality of a PC  $S_{\mathcal{C}}(\partial c)$  is that of the shrunk lattice  $\mathcal{L}$  containing the cell  $c$ , and its cell color is the color of the AQ  $Q(c)$ . Remark that the cell color is different from the color of  $\mathcal{L}$ , as shown in Table I. We refer to a primal  $c$ -colored PC as a “pc-PC.”

Remark that a given dcAQ  $q$  corresponds to two primal cells, one for each of  $\mathcal{L}^{pc_1}$  and  $\mathcal{L}^{pc_2}$  where  $c$ ,  $c_1$ , and  $c_2$  are all different colors. However, the PCs corresponding to the cells are indeed the same, comparing Fig. 6(a) and (b) as an example. We can thus regard that one AQ ( $q$ ) corresponds to one PC, and denote it as  $S_{PC}(q)$ . The support of the pc-PC  $S_{PC}(q)$  for a dcAQ  $q$  contains two pcAQs and multiple pcCQs around  $q$  as shown in Fig. 17(a)

We first consider only vacuum qubits. Since they are measured in the  $X$  basis, all PCs survive as stabilizers after the measurement step. Any  $Z$  error before the measurement or any  $X$ -measurement ( $M_X$ ) error flips several PC outcomes. Note that  $X$  errors do not affect the outcomes at all, so can be ignored. The final step for error correction is to decode errors from them and correct the errors.

An error may occur on either an AQ or a CQ. An error on a pcAQ  $q$  flips two pc-PCs sandwiching  $q$  along the time axis as shown in Fig. 17(b). An error on a pCQ  $q$  flips pr-PC, pg-PC, and pb-PC surrounding  $q$  spatially, as shown in Fig. 17(c). If both the pCQs constituting a pcL  $l$  have errors, the two pc-PCs connected by  $l$  are flipped.

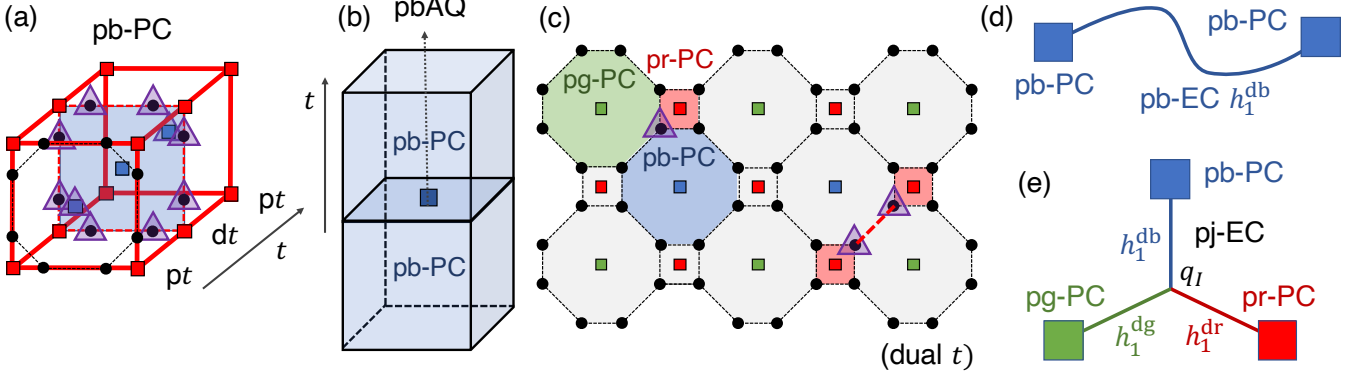


FIG. 17. (a) Explicit structure of a parity-check operator (PC), specifically a pb-PC in a 8-8-4 CCCS. Purple triangles indicate its  $X$ -support qubits. (b) A  $Z$  or  $X$ -measurement ( $M_X$ ) error on a pcAQ flips two pc-PCs sandwiching  $q$ . (c) A dual layer of a 8-8-4 CCCS is presented. Purple triangles indicate the pCQs with errors. Each  $c$ -colored face corresponds to a flipped pc-PC, where an example is shown in (a) as a blue face on the dual layer. (d) A primal blue error chain (pb-EC), where every qubit along a connected dual 1-chain  $h_1^{db}$  has an error, flips two pb-PCs located at its two ends. (e) Starting from an error on a pCQ  $q_I$ , a pj-EC is constructed by multiplying a pc-EC ending at the flipped pc-PC for each color  $c$  to the error operator. A pj-EC flips three primal PCs located at its ends.

Combining the above facts, we conclude that, if every qubit in  $Q(h_1^{dc})$  for a connected dual 1-chain  $h_1^{dc} \in H_1^{dc}$  has an error, the pc-PC  $S_{PC}(q)$  for each qubit  $q \in Q(\partial h_1^{dc})$  is flipped, as shown in Fig. 17(d). Such an error set in the vacuum is called a primal  $c$ -colored *error chain*, referred to as a “pc-EC.” Formally, a pc-EC is written as the tensor product of the  $Z$  operators on the error qubits. Furthermore, starting from an error on a pCQ, each flipped PC may be “moved” by multiplying a primal error chain of the corresponding color ending at the PC. An error set constructed by this way flips three primal PCs located at its ends and is referred to as a “pj-EC.” General error chains are obtained by connecting multiple pc-ECs for each color  $c$  and pj-ECs.

We now investigate the effects of a pc-D  $d$  to the nearby PCs. First, all primal PCs whose supports contain any defect qubit no longer survive, while dual PCs are unaffected. Such incompatible PCs may be multiplied with each others to form larger compatible stabilizers, as shown in Fig. 18 where two pg-PCs and a pr-PC are merged. Like normal PCs, these merged PCs also can detect errors, although decoding errors from PCs may get more ambiguous. Some PCs for which such multiplication is impossible have no choice but to be discarded, as the pb-PC in Fig. 18. As a consequence, a pc-EC ending at  $d$  is not detected by any PC near  $d$ .

A pc-D may make some dual CSs survive additionally. The dc-CS  $S_{CS}(f)$  for a face  $f \in \mathcal{B}_2^{dc}$ , where  $Q(\partial f)$  is in the defect as shown in Fig. 18, is compatible, thus can serve as a PC for detecting errors. We call such CSs *defect PCs*. A notable thing is that they may detect not only errors on vacuum qubits but also  $X$  or  $Z$ -measurement ( $M_Z$ ) errors on defect qubits.

We then identify nontrivial undetectable error chains, where “nontrivial” here means that they incur logical er-

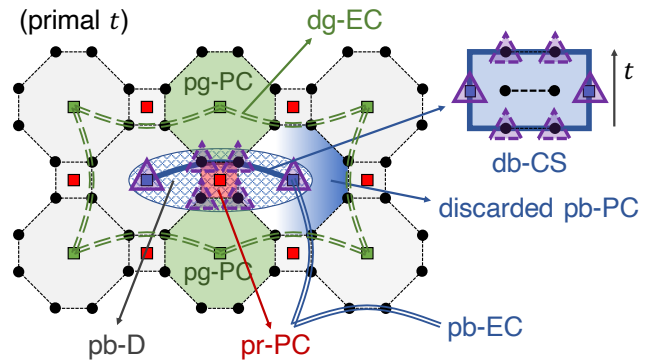


FIG. 18. PCs deformed or created due to a timelike pb-D in a 8-8-4 CCCS. A cross section of the defect on a primal layer is presented. Each purple triangle with a solid (or dashed) border indicates a defect qubit on the layer (or an adjacent dual layer). Although each of the two pg-PCs and one pr-PC marked is incompatible with the defect, their product is compatible, thus it can be used for error correction. However, the marked pb-PC cannot be merged with other PCs in such a way, thus there is no choice but to discard it, which makes a pb-EC ending at it (blue double solid line) undetectable. A dg-EC surrounding the defect (green double dashed line) located in an adjacent dual layer is another nontrivial undetectable set of errors. Some dual CSs including the presented db-CS additionally survive and can be used to detect errors in both the vacuum and defect.

rors. Such an error chain is closed or ends at defects with the same primality and color. Considering the identity gate of a primal logical qubit, the shortest error chain inducing an  $X_L$  error is a pj-EC ending at the three defects, and the shortest one inducing a  $Z_L$  error is a closed dc-EC surrounding the pc'-D ( $c' \neq c$ ), as shown schematically

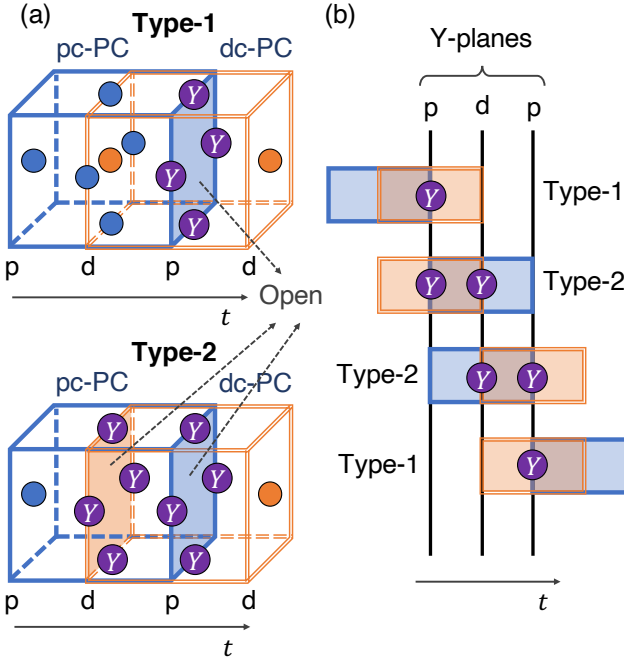


FIG. 19. (a) Two types of hybrid PCs. Each cube is a pc-PC (blue solid line) or dc-PC (orange double line) which constitutes a hybrid PC and may be open, where the colored faces indicate the open faces. Y-support qubits of the hybrid PCs are marked as purple circles, and their X-support qubits originally in the p(d)c-PCs are marked as blue (orange) circles. (b) For three consecutive Y-planes, a hybrid PC may be placed in the presented four ways. Errors in the Y-planes may be corrected using the outcomes of such hybrid PCs covering the entire Y-planes.

in Fig. 10 and explicitly in Fig. 18. Note that a closed dc-EC penetrating a defect is detected by defect PCs, although not detected by ordinary PCs. The *code distance* of a logical qubit is defined by the size of the smallest nontrivial undetectable error set, and it increases as the defects get thicker or get farther from each others.<sup>5</sup>

### B. Error correction in Y-planes

To correct errors in Y-planes, we use *hybrid* PCs defined with *open* PCs, which are visualized in Fig. 19(a)

**Definition 9 (Open PC).** For a cell  $c$  and a face  $f \in \partial c$ , an open PC is  $S_{\text{CS}}(\partial c)S_{\text{CS}}(f)$ , where  $f$  determines the

<sup>5</sup> Such an error set may not be an error chain, because errors in defects may also be nontrivial and undetectable. However, since error correction in defects gets more accurate as the defects get thicker, the dependency of the code distance to their thicknesses is still valid. It can be verified that the smallest nontrivial undetectable error set containing only defect qubits completely covers a cross section of the defect, thus its size is roughly a quadratic function of the circumference of the defect.

direction toward which it is open.

**Definition 10 (Hybrid PC).** A hybrid PC is the product of primal and dual PCs with the same color which are adjacent along the time axis and may be open toward each other. It is type-1 if one of the two composing PCs is open, while it is type-2 if both of them are open.

Remark that CQs in Y-planes are measured in the  $Y$  basis, thus ordinary PCs whose supports contain those CQs are incompatible with the  $Y$ -measurements. Instead of them, we use hybrid PCs whose  $Y$ -supports are on the Y-planes, as shown in Fig. 19(b). Error correction in the Y-planes is done with a set of hybrid PCs covering the entire Y-planes.

## VI. CALCULATIONS

### A. Resource overhead

We now calculate and compare the resource overhead of MBQC via RTCSs or CCCSs. For each case, we consider a periodic hexagonal arrangement of parallel timelike primal defects, where primal logical qubits with the code distances of  $d$  are compactly packed in the space. In other words, the intervals of the arrangement are determined to minimize the number of physical qubits per logical qubit while keeping all the possible nontrivial undetectable error chains to contain  $d$  or more qubits. We present such arrangements of defects in Appendix A.

Table III shows the calculated numbers of physical qubits ( $n$ ) and CZ gates ( $N_{\text{CZ}}$ ) per layer in terms of  $d$  and the number of logical qubits ( $k$ ), considering the optimal hexagonal arrangements. It is worth noticing that MBQC via CCCSs is definitely more resource-efficient than MBQC via RTCSs;  $n/k$  is about 1.7–1.8 times smaller for CCCSs than for RTCSs. Note that the compact packing of logical qubits may be unrealistic; extra spaces may be needed for implementing logical gates besides the identity gate.

TABLE III. Resource overhead of MBQC via RTCSs or CCCSs, evaluated by the numbers of physical qubits ( $n$ ) and CZ gates ( $N_{\text{CZ}}$ ) per layer in terms of the code distance ( $d$ ) and the number of logical qubits ( $k$ ), regarding optimal hexagonal arrangements of parallel timelike primal defects. Only the leading-order terms on  $d$  are presented. Two types of color codes are considered: the 8-8-4 and 6-6-6 lattices.

Types of cluster states	$n/k$	$N_{\text{CZ}}/k$
RTCS	$\approx 6.6d^2$	$\approx 13.1d^2$
8-8-4 CCCS	$\approx 3.9d^2$	$\approx 10.5d^2$
6-6-6 CCCS	$\approx 3.7d^2$	$\approx 9.8d^2$

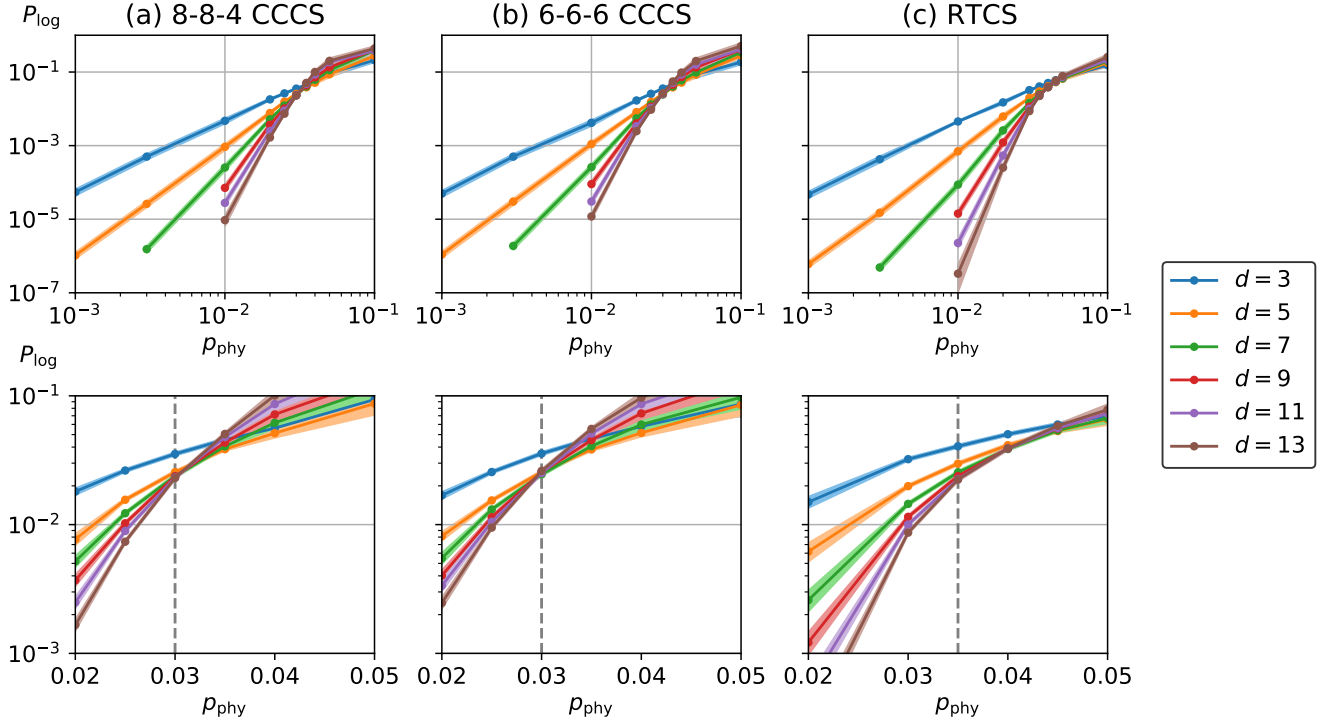


FIG. 20.  $Z_L$  error probability  $P_{\log}$  versus physical-level error probability  $p_{\text{phys}} = p_Z + p_{M_X} - p_Z p_{M_X}$ , where  $p_Z$  ( $p_{M_X}$ ) is the  $Z$  ( $X$ -measurement) error probability on vacuum qubits, for different code distances with respect to (a) 8-8-4 CCCSs, (b) 6-6-6 CCCSs, and (c) RTCSs. The graphs in the upper row show the results for  $0.001 \leq p_{\text{phys}} \leq 0.1$ , and those in the lower row show the results near the threshold values. Pale areas around the lines indicate the 99% confidence intervals of  $P_{\log}$ . The error thresholds are calculated as approximately 3.0% for both types of CCCSs and 3.5% for RTCSs, which are shown as grey dashed lines.

## B. Error thresholds

We numerically calculate and compare error thresholds of MBQC via RTCSs and CCCSs.

### 1. Error model

We assume a simple error model where vacuum qubits have  $Z$  ( $M_X$ ) errors independently with the same probability  $p_Z$  ( $p_{M_X}$ ). Since a  $Z$  error just before the measurement and an  $M_X$  error have the same effect, it is enough to consider the net error probability  $p_{\text{phy}} := p_Z + p_{M_X} - p_Z p_{M_X}$ . Note that  $X$  errors on the vacuum qubits do not affect the  $X$ -measurement results at all, thus we neglect them.

### 2. Simulation methods

For each simulation with a code distance of  $d$ , we consider the logical identity gate of a primal logical qubit covering consecutive  $2T+1$  layers with  $T = 4d+1$  starting from a primal layer. Simplified defect models presented

in Appendix B 1 are used, instead of considering big areas containing the entire defects. We calculate the  $Z_L$  error probability per layer with the Monte Carlo method; we repeat a sampling cycle many times enough to obtain a desired confidence interval of the  $Z_L$  error probability. Each cycle is structured as follows.

We first prepare a cluster state whose shape and size are determined by  $d$  and  $T$ . Here we assume perfect preparation, namely, no qubit losses or failures of CZ gates. Errors are then randomly assigned to primal qubits with a given probability  $p_{\text{phy}}$ , except those in the first and final layers to prevent error chains ending at these layers. After that, the outcomes of primal PCs are calculated, then decoded to locate errors. Edmonds' minimum-weight perfect matching (MWPM) algorithm [61–63] via Blossom V software [64] is used for decoding (once for RTCSs and six times for CCCSs), where the details are presented in Appendix B 2. We then identify primal error chains connecting different defects which incur  $Z_L$  errors by comparing the assigned and decoded errors. We count such error chains while repeating the cycles and obtain the  $Z_L$  error probability per layer  $P_{\log}$ . The error threshold  $p_{\text{thrs}}$  is obtained from the calculated  $P_{\log}$  results for different values of  $d$  and  $p_{\text{phy}}$ ;  $P_{\log}$  decreases as  $d$  increases if  $p_{\text{phy}} < p_{\text{thrs}}$  and vice versa otherwise.

### 3. Results

Figure 20 shows the results of the simulations. The obtained error thresholds are  $p_{\text{thrs}} \approx 3.0\%$  for 8-8-4 and 6-6-6 CCCSs and  $p_{\text{thrs}} \approx 3.5\%$  for RTCSs. The values for CCCSs are slightly lower than the value for RTCSs, but they have similar orders of magnitude.

## VII. REMARKS

In this paper, we have proposed a new topological measurement-based quantum computation (MBQC) scheme via color-code-based cluster states (CCCSs). We have shown that our scheme is comparable with or even better than the conventional scheme via Raussendorf's 3D cluster states (RTCSs) [38, 41–43], in the three aspects mentioned at the very beginning:

1. *Universality.* Initialization and measurements of logical qubits and all the elementary logical gates constituting a universal set of gates (CNOT, Hadamard, phase, and  $T$  gates) can be implemented via appropriate placement of defects and Y-planes. We described each one of them explicitly in Sec. IV.
2. *Fault-tolerance.* We suggested the error correction scheme for each area of qubits in Sec. V. We further verified in Sec. VI B that the error thresholds for  $Z$  or  $X$ -measurement errors have a similar order of magnitude comparing with the value for RTCSs.
3. *Resource-efficiency.* Contrary to the case of using RTCSs, the Hadamard and phase gates do not require state distillation as shown in Sec. IV D, thanks to the nature of the self-duality of the 2D color codes. Since state distillation is very costly [22, 36, 38], the amount of required resources is significantly smaller than the case of using RTCSs. Moreover, we found out in Sec. VI A that the minimal number of physical qubits per logical qubits is about 1.7–1.8 times smaller for our scheme, comparing to the value for RTCSs.

We particularly emphasize the last aspect as a definite improvement compared to MBQC via RTCSs, which makes CCCSs competitive alternatives to RTCSs.

Our work has several limitations. First, the logical  $T$  gate still needs costly state distillation. Some methods to significantly reduce the cost of distillation have been proposed, such as using logical qubits with low code distances as ancilla qubits [65] or exploiting redundant ancilla encoding and flag qubits [66]. Moreover, 3D gauge color codes [28–35] enables implementation of a universal set of gates without distillation. It may be possible to translate these protocols to be applicable for our MBQC scheme. We also assume the perfect preparation of states, which is unrealistic. It is unclear how much the

fault-tolerance gets weaker if we consider qubits losses or failures of CZ gates, which is particularly related to photon losses in optical systems. It will be interesting future works to further investigate and resolve these problems.

Lastly, we would like to mention a recent work on a topological MBQC scheme using the Walker-Wang model for the 3-Fermion anyon theory [67]. It provides a general framework on universal QC with defect braiding, which produces the MBQC scheme via RTCSs as an example. There may be some connections between this work and our scheme, which is worth further investigation.

## ACKNOWLEDGMENTS

This work was supported by the National Research Foundation of Korea (NRF-2019M3E4A1080074, NRF-2020R1A2C1008609, NRF-2020K2A9A1A06102946) via the Institute of Applied Physics at Seoul National University and by the Ministry of Science and ICT, Korea, under the ITRC (Information Technology Research Center) support program (IITP-2020-0-01606) supervised by the IITP (Institute of Information & Communications Technology Planning & Evaluation).

## Appendix A: Details on calculation of resource overhead

Here we calculate the resource overhead of MBQC via RTCSs or CCCSs, namely, the numbers of physical qubits ( $n$ ) and required CZ gates ( $N_{\text{CZ}}$ ) per layer in terms of the code distance ( $d$ ) and the number of logical qubits ( $k$ ), which are presented in Table III and Sec. VI A. We consider hexagonal arrangements of parallel timelike primal defects, where every error chain connecting different defects or surrounding a defect has  $d$  or more qubits. We need to find the optimal intervals minimizing  $n/k$ .

We first define the coordinate systems for the analysis. The  $x$  and  $y$  axes are presented in Fig. 1(b) for RTCSs and Fig. 2 for the two types of CCCSs. The unit length is the length of a side of a unit cell for RTCSs, the distance between adjacent prAQ and pgAQ for 8-8-4 CCCSs, and half the distance between two adjacent AQs with the same color for 6-6-6 CCCSs.

The optimal arrangement in a RTCS is shown in Fig. 21(a). It is straightforward to obtain the intervals, considering that the shortest error chain connecting  $(0, 0)$  and  $(x, y)$  contains  $|x| + |y| + O(1)$  qubits. Note that we calculate only their leading-order terms on  $d$ . The area occupied by a logical qubit is thus about  $\frac{35}{16}d^2$ , and since a unit area contains three qubits and six CZ gates, we get  $n/k \approx 6.6d^2$  and  $N_{\text{CZ}}/k \approx 13.1d^2$ . Note that, for each CQ, we count only one of the two related CZ gates with other CQs in the adjacent layers.

It is more tricky to obtain the optimal arrangements in 8-8-4 or 6-6-6 CCCSs. Figure 21(b) shows the concerned hexagonal arrangement with five variables  $(\alpha, \beta, \gamma, \delta, \epsilon)$

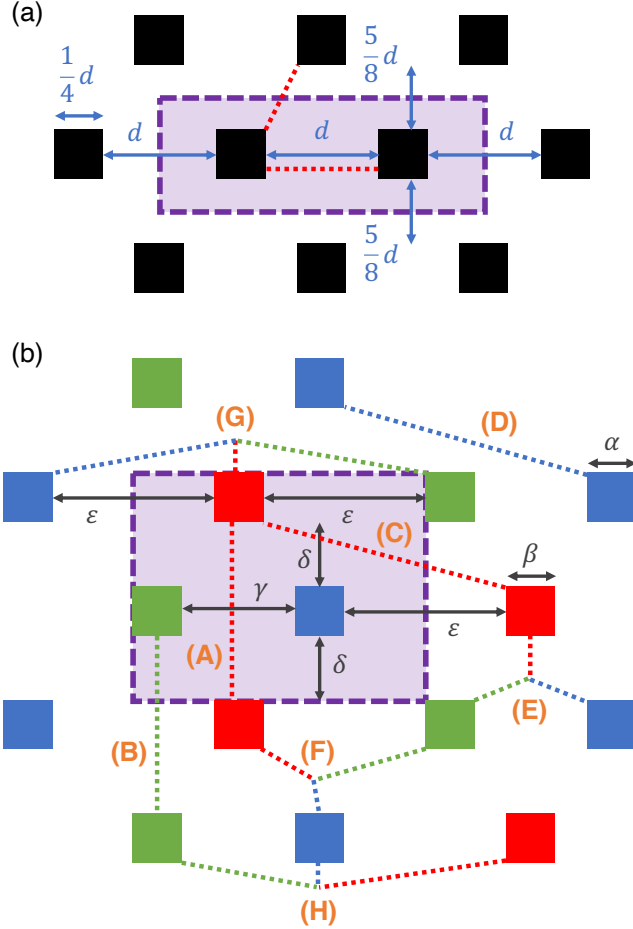


FIG. 21. Arrangements of primal defects penetrating a layer for calculating resource overhead of MBQC via (a) RTCSSs or (b) CCCSs. Each black, red, green, or blue square is a defect, where its color means the color of the defect if it is in (b). Each purple rectangle surrounded by dashed lines is an area occupied by a logical qubit. Dotted lines indicate all the possible types of error chains which may be the shortest ones, which are used for obtaining the values of the marked intervals minimizing the area of a logical qubit. Note that, in (b), counterparts of some error chains regarding the exchange of blue and green defects are omitted, since the two lattices (8-8-4 and 6-6-6) which we concern have symmetry on those defects. The optimal intervals for RTCSSs are directly presented in (a). For CCCSs, they are  $(\alpha, \beta, \gamma, \delta, \epsilon) = (\frac{1}{4}d, \frac{1}{4}d, 0, \frac{1}{2}d, \frac{1}{2}d)$  for 8-8-4 and  $(\alpha, \beta, \gamma, \delta, \epsilon) \approx (0.23d, 0.23d, 0.38d, 0.53d, 0.38d)$  for 6-6-6. Here, the unit length is a side of a unit cell in RTCSSs (see Fig. 1(b)), the distance between adjacent prAQ and pgAQ in 8-8-4 CCCSs (see Fig. 4(a)), and half the distance between two adjacent prAQs in 6-6-6 CCCSs (see Fig. 2(b)).

for the intervals considering the symmetry. We consider only the leading-order terms of their values on  $d$  as well.

We first look at 8-8-4 CCCSs. The shortest pr-EC connecting  $(0, 0)$  and  $(x, y)$  contains  $2 \max(x, y) + O(1)$  qubits, and the shortest pg-EC or pb-EC connecting them contains  $|x| + |y| + O(1)$  qubits. The thicknesses of the de-

fects,  $\alpha$  and  $\beta$ , can be derived from the shortest pg-EC or pb-EC surrounding each defect:  $\alpha = \beta = \frac{1}{4}d$ . The following eight inequalities are derived from the eight possible types (A)–(H) of error chain in Fig. 21(b):

$$\begin{aligned}
 \text{(A)} \quad & \delta \geq \frac{1}{8}d, \\
 \text{(B)} \quad & \delta \geq \frac{3}{8}d, \\
 \text{(C)} \quad & \max\left(\gamma + 2\epsilon + \frac{1}{4}d, 2\delta\right) \geq d, \\
 \text{(D)} \quad & \gamma + 2\delta + 2\epsilon \geq \frac{7}{4}d, \\
 \text{(E)} \quad & \gamma + 2\delta \geq d, \\
 \text{(F)} \quad & \delta + \epsilon + \frac{1}{2} \max\left(\gamma - \frac{1}{4}d, 0\right) \geq d, \\
 \text{(G)} \quad & \epsilon \geq \frac{3}{8}d, \\
 \text{(H)} \quad & \gamma + 2\epsilon \geq \frac{3}{4}d.
 \end{aligned}$$

Note that, to get the inequalities corresponding to (E)–(H), the points at which three error chains meet should be placed carefully. It is straightforward to see that placing each point just next to the red defect minimizes the length of the error chain. The area  $S$  occupied by a logical qubit is written as

$$S \approx \left(\alpha + \frac{\beta}{2} + \frac{\gamma}{2} + \epsilon\right)(2\delta + \alpha + \beta). \quad (\text{A1})$$

Minimizing  $S$  subject to the above inequalities, we get  $S \approx \frac{21}{16}d^2$  where the corresponding intervals are  $(\alpha, \beta, \gamma, \delta, \epsilon) = (\frac{1}{4}d, \frac{1}{4}d, 0, \frac{1}{2}d, \frac{1}{2}d)$ . A unit area contains three qubits and eight CZ gates, thus we get  $n/k \approx 3.9d^2$  and  $N_{\text{CZ}}/k \approx 10.5d^2$ .

The optimal arrangement for 6-6-6 CCCSs also can be derived similarly. The shortest error chain connecting  $(0, 0)$  and  $(x, y)$  for  $x, y \geq 0$  contains  $\max\left(x + \frac{1}{\sqrt{3}}y, \frac{2}{\sqrt{3}}y\right) + O(1)$  qubits. We thus get  $\alpha = \beta = (\sqrt{3} - \frac{3}{2})d \approx 0.23d$ , considering an error chain surrounding a defect. The following inequalities are derived for each type of error chain:

$$\begin{aligned}
 \text{(A), (B)} \quad & \delta \geq \frac{3 - \sqrt{3}}{4}d, \\
 \text{(C), (D)} \quad & \max\left(\frac{1}{2}\gamma + \frac{1}{\sqrt{3}}\delta + \epsilon + \frac{1}{2}\alpha, \frac{2}{\sqrt{3}}\delta\right) \geq d, \\
 \text{(E)} \quad & \gamma + \frac{2}{\sqrt{3}}\delta \geq d, \\
 \text{(F)} \quad & \epsilon + \frac{2}{\sqrt{3}}\delta \geq d, \\
 \text{(G)} \quad & 2\epsilon \geq d - \alpha, \\
 \text{(H)} \quad & \epsilon + \gamma \geq d - \alpha.
 \end{aligned}$$

Minimizing  $S$  in Eq. (A1) subject to the inequalities, we get  $S \approx 1.42d^2$  where the corresponding intervals are

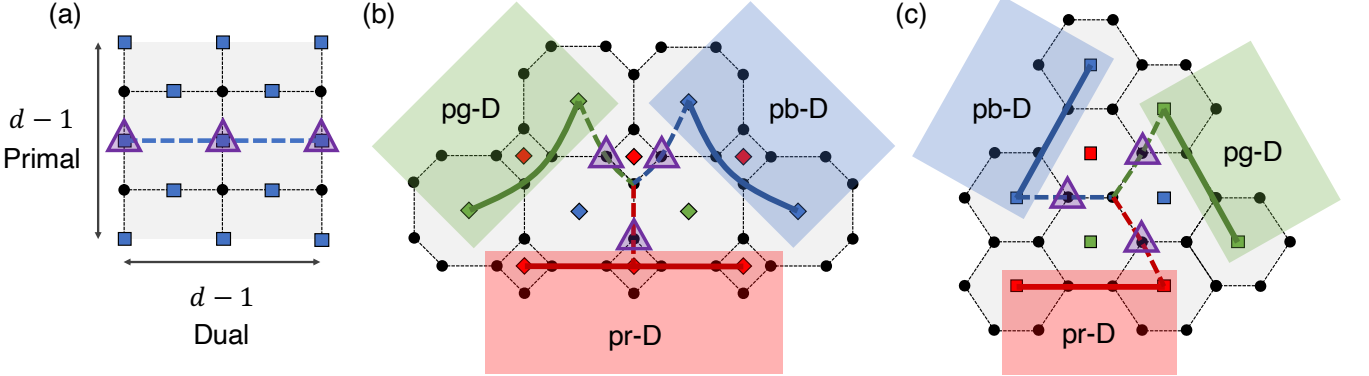


FIG. 22. Structure of a layer in the simplified defect model for the simulation regarding (a) RTCSSs, (b) 8-8-4 CCCSSs, or (c) 6-6-6 CCCSSs, particularly when the code distance is  $d = 3$ . In (a), blue squares (black circles) indicate primal (dual) qubits. In (b) and (c), a colored solid line is a boundary corresponding to that color, which can be regarded as a part of a defect. For all of them, dashed lines are examples of primal error chains incurring  $Z_L$  errors. Purples triangles indicate the qubits in the error chains, which show that the code distances are three. Defect models for  $d > 3$  can be constructed analogously by increasing the distances between the boundaries while keeping their shapes.

$(\alpha, \beta, \gamma, \delta, \epsilon) \approx (0.23d, 0.23d, 0.38d, 0.53d, 0.38d)$ . A unit area contains  $3\sqrt{3}/2$  qubits and  $4\sqrt{3}$  CZ gates, thus we get  $n/k \approx 3.7d^2$  and  $N_{\text{CZ}}/k \approx 9.8d^2$ .

## Appendix B: Details on calculation of error thresholds

We here present some details on the calculation of error thresholds presented in Sec. VI B.

### 1. Simplified defect models

As mentioned in the main text, we simplify the defect models for efficient simulations. Instead of considering big regions containing the entire defects, we consider only regions surrounded by boundaries corresponding to the defects. That is, we only take account of error chains located in the “inner” regions surrounded by the defects. Since those error chains are strictly shorter than error chains passing outside the regions, we conjecture that this assumption does not affect the resulting  $Z_L$  error probabilities much.

Figure 22 shows single layers of the three simplified defect models for the simulations regarding RTCSSs, 8-8-4 CCCSSs, and 6-6-6 CCCSSs, respectively. Each layer of the concerned RTCSSs has the shape of a square with a side length of  $d-1$  in the units of cells for the code distance  $d$ , where the boundaries are of different types (primal and dual). Any error chain connecting the two primal boundaries incurs a  $Z_L$  error. For CCCSSs, we consider a region surrounded by three boundaries of different colors, where each boundary can be regarded as a part of a defect. Any error chain connecting the three boundaries incurs a  $Z_L$  error.

## 2. Decoding methods

### a. Raussendorf’s 3D cluster states

In a RTCSS, the PC outcomes are decoded to locate errors at vacuum qubits via Edmonds’ minimum-weight perfect matching algorithm (MWPM) [61–63], as frequently used in the literature [41, 44, 45, 68]. Remark that an error chain flips at most two PCs located at its ends, and if it flips one PC, it ends at the boundary. Hence, our goal is to figure out the most probable set of error chains based on the PC outcomes.

The decoding procedure is briefly summarized as follows. First, a graph is constructed from the PC outcomes. The vertex set of the graph contains two vertices for each flipped PC: one is the PC itself and the other is the “boundary vertex.” An edge is connected between each pair of different PCs, each pair of a PC and the corresponding boundary vertex, and each pair of different boundary vertices. A “weight” value is assigned to each edge as follows. If both the vertices are PCs, the weight is the number of qubits in the shortest path between them. If only one of them is a PC, the weight is the number of qubits in the shortest path between the PC and the closest boundary. If both of them are boundary vertices, the weight is zero.

We use the MWPM algorithm via Blossom V software [64] to search for a set of edges of the graph constructed above which covers all the vertices, does not contain duplicated vertices, and minimizes the total weight. Each edge in the resulting set corresponds to a pair of PCs flipped by an error chain or a PC flipped by an error chain ending at the boundary, unless the edge connects two boundary vertices, which is ignored. We can thus locate errors from the error chain along the shortest path for each edge. Since the total weight is minimized, we get the smallest of the sets of edges producing the same PC

outcomes, which is the most probable assuming that the error probabilities are independent and the same between qubits.

### b. Color-code-based cluster states

The decoding method for RTCSs is not directly applicable to CCCSs, since an error in a CCCS flips at most three PCs, unlike the case of a RTCS. The decoding for each sample requires the application of the MWPM algorithm six times.

First, the outcomes of **pb**-PCs and **pg**-PCs are decoded to find the faces in  $\mathcal{L}^{\text{pr}}$  with odd numbers of errors, via

the method analogous to that for RTCSs. This is possible since each of such faces flips at most two (blue or green) PCs like an error in a RTCS. Remark that each face in  $\mathcal{L}^{\text{pr}}$  corresponds to a **pbAQ**, **pgAQ**, or **prL**. Errors at **pbAQs** and **pgAQs** are thus obtained from this process.

Next, the left results for **prLs** and the outcomes of **pr-PCs** are decoded to locate errors at **prAQs** and **pCQs**, regarding the parity of the number of errors in each **prL** as a PC. This is possible since an error at a **prAQ** or **pCQ** flips at most two PCs (**pr-PCs** and **prLs**).

All the errors are finally located by the above process. However, to make the decoding more accurate, we repeat it for  $\mathcal{L}^{\text{pb}}$  and  $\mathcal{L}^{\text{pg}}$  analogously and select the smallest set of decoded errors among the three results.

---

[1] A. Galindo and M. A. Martín-Delgado, Information and computation: Classical and quantum aspects, *Rev. Mod. Phys.* **74**, 347 (2002).

[2] M. A. Nielsen and I. L. Chuang, *Quantum Computation and Quantum Information* (Cambridge University Press, 2010).

[3] P. W. Shor, Scheme for reducing decoherence in quantum computer memory, *Phys. Rev. A* **52**, R2493 (1995).

[4] C. H. Bennett, D. P. DiVincenzo, J. A. Smolin, and W. K. Wootters, Mixed-state entanglement and quantum error correction, *Phys. Rev. A* **54**, 3824 (1996).

[5] R. Laflamme, C. Miquel, J. P. Paz, and W. H. Zurek, Perfect quantum error correcting code, *Phys. Rev. Lett.* **77**, 198 (1996).

[6] A. R. Calderbank and P. W. Shor, Good quantum error-correcting codes exist, *Phys. Rev. A* **54**, 1098 (1996).

[7] A. Steane, Multiple-particle interference and quantum error correction, *P. Roy. Soc. Lond. A Mat.* **452**, 2551 (1996).

[8] H. Bombín, Topological codes, in *Quantum Error Correction*, edited by D. A. Lidar and T. A. Brun (Cambridge, 2013) Chap. 19, pp. 455–481.

[9] D. G. Cory, M. D. Price, W. Maas, E. Knill, R. Laflamme, W. H. Zurek, T. F. Havel, and S. S. Somaroo, Experimental quantum error correction, *Phys. Rev. Lett.* **81**, 2152 (1998).

[10] J. Chiaverini, D. Leibfried, T. Schaetz, M. D. Barrett, R. B. Blakestad, J. Britton, W. M. Itano, J. D. Jost, E. Knill, C. Langer, R. Ozeri, and D. J. Wineland, Realization of quantum error correction, *Nature* **432**, 602 (2004).

[11] P. Schindler, J. T. Barreiro, T. Monz, V. Nebendahl, D. Nigg, M. Chwalla, M. Hennrich, and R. Blatt, Experimental repetitive quantum error correction, *Science* **332**, 1059 (2011).

[12] M. D. Reed, L. DiCarlo, S. E. Nigg, L. Sun, L. Frunzio, S. M. Girvin, and R. J. Schoelkopf, Realization of three-qubit quantum error correction with superconducting circuits, *Nature* **482**, 382 (2012).

[13] D. Nigg, M. Müller, E. A. Martinez, P. Schindler, M. Hennrich, T. Monz, M. A. Martin-Delgado, and R. Blatt, Quantum computations on a topologically encoded qubit, *Science* **345**, 302 (2014).

[14] A. D. Córcoles, E. Magesan, S. J. Srinivasan, A. W. Cross, M. Steffen, J. M. Gambetta, and J. M. Chow, Demonstration of a quantum error detection code using a square lattice of four superconducting qubits, *Nat. Commun.* **6**, 1 (2015).

[15] J. Kelly, R. Barends, A. G. Fowler, A. Megrant, E. Jeffrey, T. C. White, D. Sank, J. Y. Mutus, B. Campbell, Y. Chen, B. Chiaro, A. Dunsworth, I.-C. Hoi, C. Neill, P. J. J. O’Malley, C. Quintana, P. Roushan, A. Vainsencher, J. Wenner, A. N. Cleland, and J. M. Martinis, State preservation by repetitive error detection in a superconducting quantum circuit, *Nature* **519**, 66 (2015).

[16] N. Ofek, A. Petrenko, R. Heeres, P. Reinhold, Z. Leghtas, B. Vlastakis, Y. Liu, L. Frunzio, S. M. Girvin, L. Jiang, M. Mirrahimi, M. H. Devoret, and R. J. Schoelkopf, Extending the lifetime of a quantum bit with error correction in superconducting circuits, *Nature* **536**, 441 (2016).

[17] C. K. Andersen, A. Remm, S. Lazar, S. Krinner, N. Lacroix, G. J. Norris, M. Gabureac, C. Eichler, and A. Wallraff, Repeated quantum error detection in a surface code, *Nat. Phys.* **16**, 875 (2020).

[18] A. Y. Kitaev, Quantum computations: algorithms and error correction, *Russ. Math. Surv.* **52**, 1191 (1997).

[19] S. B. Bravyi and A. Y. Kitaev, Quantum codes on a lattice with boundary, *arXiv preprint quant-ph/9811052* (1998).

[20] E. Dennis, A. Kitaev, A. Landahl, and J. Preskill, Topological quantum memory, *J. Math. Phys.* **43**, 4452 (2002).

[21] A. Y. Kitaev, Fault-tolerant quantum computation by anyons, *Ann. Phys.* **303**, 2 (2003).

[22] A. G. Fowler, A. M. Stephens, and P. Groszkowski, High-threshold universal quantum computation on the surface code, *Phys. Rev. A* **80**, 052312 (2009).

[23] H. Bombin and M. A. Martin-Delgado, Quantum measurements and gates by code deformation, *J. Phys. A: Math. Theor.* **42**, 095302 (2009).

[24] A. G. Fowler, M. Mariantoni, J. M. Martinis, and A. N. Cleland, Surface codes: Towards practical large-scale quantum computation, *Phys. Rev. A* **86**, 032324 (2012).

[25] B. M. Terhal, Quantum error correction for quantum memories, *Rev. Mod. Phys.* **87**, 307 (2015).

[26] H. Bombin and M. A. Martin-Delgado, Topological quantum distillation, *Phys. Rev. Lett.* **97**, 180501 (2006).

[27] A. G. Fowler, Two-dimensional color-code quantum com-

putation, Phys. Rev. A **83**, 042310 (2011).

[28] H. Bombin and M. A. Martin-Delgado, Topological computation without braiding, Phys. Rev. Lett. **98**, 160502 (2007).

[29] H. Bombin and M. A. Martin-Delgado, Exact topological quantum order in  $d = 3$  and beyond: Branyons and brane-net condensates, Phys. Rev. B **75**, 075103 (2007).

[30] H. Bombín, Gauge color codes: optimal transversal gates and gauge fixing in topological stabilizer codes, New J. Phys. **17**, 083002 (2015).

[31] A. Kubica and M. E. Beverland, Universal transversal gates with color codes: A simplified approach, Phys. Rev. A **91**, 032330 (2015).

[32] F. H. E. Watson, E. T. Campbell, H. Anwar, and D. E. Browne, Qudit color codes and gauge color codes in all spatial dimensions, Phys. Rev. A **92**, 022312 (2015).

[33] A. Kubica, M. E. Beverland, F. Brandão, J. Preskill, and K. M. Svore, Three-dimensional color code thresholds via statistical-mechanical mapping, Phys. Rev. Lett. **120**, 180501 (2018).

[34] H. Bombin, 2d quantum computation with 3d topological codes, arXiv preprint arXiv:1810.09571 (2018).

[35] H. Bombin, Transversal gates and error propagation in 3d topological codes, arXiv preprint arXiv:1810.09575 (2018).

[36] S. Bravyi and A. Kitaev, Universal quantum computation with ideal clifford gates and noisy ancillas, Phys. Rev. A **71**, 022316 (2005).

[37] C. Jones, Multilevel distillation of magic states for quantum computing, Phys. Rev. A **87**, 042305 (2013).

[38] R. Raussendorf, J. Harrington, and K. Goyal, Topological fault-tolerance in cluster state quantum computation, New J. Phys. **9**, 199 (2007).

[39] R. Raussendorf and H. J. Briegel, A one-way quantum computer, Phys. Rev. Lett. **86**, 5188 (2001).

[40] R. Raussendorf, D. E. Browne, and H. J. Briegel, Measurement-based quantum computation on cluster states, Phys. Rev. A **68**, 022312 (2003).

[41] R. Raussendorf, J. Harrington, and K. Goyal, A fault-tolerant one-way quantum computer, Ann. Phys. **321**, 2242 (2006).

[42] R. Raussendorf and J. Harrington, Fault-tolerant quantum computation with high threshold in two dimensions, Phys. Rev. Lett. **98**, 190504 (2007).

[43] A. G. Fowler and K. Goyal, Topological cluster state quantum computing, Quantum Info. Comput. **9**, 721–738 (2009).

[44] S. D. Barrett and T. M. Stace, Fault tolerant quantum computation with very high threshold for loss errors, Phys. Rev. Lett. **105**, 200502 (2010).

[45] A. C. Whiteside and A. G. Fowler, Upper bound for loss in practical topological-cluster-state quantum computing, Phys. Rev. A **90**, 052316 (2014).

[46] Y. Li, S. D. Barrett, T. M. Stace, and S. C. Benjamin, Fault tolerant quantum computation with nondeterministic gates, Phys. Rev. Lett. **105**, 250502 (2010).

[47] M. A. Nielsen, Optical quantum computation using cluster states, Phys. Rev. Lett. **93**, 040503 (2004).

[48] C. M. Dawson, H. L. Haselgrove, and M. A. Nielsen, Noise thresholds for optical cluster-state quantum computation, Phys. Rev. A **73**, 052306 (2006).

[49] N. C. Menicucci, P. van Loock, M. Gu, C. Weedbrook, T. C. Ralph, and M. A. Nielsen, Universal quantum computation with continuous-variable cluster states, Phys. Rev. Lett. **97**, 110501 (2006).

[50] S. J. Devitt, A. G. Fowler, A. M. Stephens, A. D. Green-tree, L. C. L. Hollenberg, W. J. Munro, and K. Nemoto, Architectural design for a topological cluster state quantum computer, New J. Phys. **11**, 083032 (2009).

[51] D. A. Herrera-Martí, A. G. Fowler, D. Jennings, and T. Rudolph, Photonic implementation for the topological cluster-state quantum computer, Phys. Rev. A **82**, 032332 (2010).

[52] K. Fujii and Y. Tokunaga, Fault-tolerant topological one-way quantum computation with probabilistic two-qubit gates, Phys. Rev. Lett. **105**, 250503 (2010).

[53] C. R. Myers and T. C. Ralph, Coherent state topological cluster state production, New J. Phys. **13**, 115015 (2011).

[54] X.-C. Yao, T.-X. Wang, H.-Z. Chen, W.-B. Gao, A. G. Fowler, R. Raussendorf, Z.-B. Chen, N.-L. Liu, C.-Y. Lu, Y.-J. Deng, Y.-A. Chen, and J.-W. Pan, Experimental demonstration of topological error correction, Nature **482**, 489 (2012).

[55] M. Gimeno-Segovia, P. Shadbolt, D. E. Browne, and T. Rudolph, From three-photon greenberger-horne-zeilinger states to ballistic universal quantum computation, Phys. Rev. Lett. **115**, 020502 (2015).

[56] Y. Li, P. C. Humphreys, G. J. Mendoza, and S. C. Benjamin, Resource costs for fault-tolerant linear optical quantum computing, Phys. Rev. X **5**, 041007 (2015).

[57] S. Omkar, Y. S. Teo, and H. Jeong, Resource-efficient topological fault-tolerant quantum computation with hybrid entanglement of light, Phys. Rev. Lett. **125**, 060501 (2020).

[58] A. Bolt, G. Duclos-Cianci, D. Poulin, and T. M. Stace, Foliated quantum error-correcting codes, Phys. Rev. Lett. **117**, 070501 (2016).

[59] A. Bolt, D. Poulin, and T. M. Stace, Decoding schemes for foliated sparse quantum error-correcting codes, Phys. Rev. A **98**, 062302 (2018).

[60] B. J. Brown and S. Roberts, Universal fault-tolerant measurement-based quantum computation, Phys. Rev. Research **2**, 033305 (2020).

[61] J. Edmonds, Paths, trees, and flowers, Can. J. Math. **17**, 449 (1965).

[62] J. Edmonds, Maximum matching and a polyhedron with 0, 1-vertices, J. Res. Nat. Bur. Stand. B **69**, 55 (1965).

[63] A. G. Fowler, Minimum weight perfect matching of fault-tolerant topological quantum error correction in average  $O(1)$  parallel time, Quantum Info. Comput. **15**, 145–158 (2015).

[64] V. Kolmogorov, Blossom v: a new implementation of a minimum cost perfect matching algorithm, Math. Program. Comput. **1**, 43 (2009).

[65] D. Litinski, Magic State Distillation: Not as Costly as You Think, Quantum **3**, 205 (2019).

[66] C. Chamberland and K. Noh, Very low overhead fault-tolerant magic state preparation using redundant ancilla encoding and flag qubits, npj Quant. Inf. **6**, 1 (2020).

[67] S. Roberts and D. J. Williamson, 3-fermion topological quantum computation, arXiv preprint arXiv:2011.04693 (2020).

[68] A. G. Fowler, A. C. Whiteside, A. L. McInnes, and A. Rabbani, Topological code autotune, Phys. Rev. X **2**, 041003 (2012).